Crustal structure of the Juan de Fuca Ridge as determined from deep towed seismic reflection profiles

by

STUART DENNY

A thesis submitted in partial fulfillment
of the requirements for the degree of

Master of Science

University of Washington

1988

Approved by B. Tan
(Chairperson of Supervisory Committee)

Program Authorized
to Offer Degree Geophysics

Date 3-18-88

Master's Thesis

In presenting this thesis in partial fulfillment of the requirements for a Master's degree at the University of Washington, I agree that the Library shall make its copies freely available for inspection. I further agree that extensive copying of this thesis is allowable only for scholarly purposes, consistent with "fair use" as prescribed in the U. S. Copyright Law. Any other reproduction for any purposes or by any means shall not be allowed without my written permission.

Signature Stuart Dorny

Date 3-18-88

University of Washington

Abstract

CRUSTAL STRUCTURE OF THE JUAN DE FUCA RIDGE AS DETERMINED FROM DEEP TOWED SEISMIC REFLECTION PROFILES

by Stuart Denny

Chairperson of the Supervisory Committee: Professor Brian T. R. Lewis

Graduate Program in Geophysics

The geologic structure of oceanic crust is the product of processes occurring at mid-ocean ridge crests. In order to gain insight into the nature of ridge crest processes, six airgun seismic reflection profiles were collected from two areas on the Juan de Fuca Ridge; three from the southern Juan de Fuca, and three from the Endeavour Segment. Processing of the profiles included deconvolution, migration, and automatic gain control. The final processed profiles all show similar features, which do not appear to be processing artifacts or other non-structural features. The features on the profiles occur at a depth of -3.5 kilometers, and may be reflections from layered gabbros. No firm evidence is found in the data for the existence of a steady-state magma chamber on the Juan de Fuca Ridge. This supports models of crustal generation which involve intermittent magma chambers. The Deep Tow seismic reflection system used is shown to be capable of imaging crustal structure at mid-ocean ridge crests.

TABLE OF CONTENTS

LIST OF FIGURES

LIST OF FIGURES (continued)

LIST OF TABLES

ACKNOWLEDGEMENTS

I would like to thank the members of my Supervisory Committe for their help: Professor Brian T. R. Lewis, Professor Stephen D. Malone, and Assistant Professor Adam Schultz. In particular I would like to thank Professor Lewis for his patience, and for conceiving of this research and obtaining the funding for it. General thanks are in order for the faculty, staff and students of both the Geophysics Program and the School of Oceanography of the University of Washington. I would also like to extend thanks to the captains and crews of the R/V's Wecoma and Thomas G. Thompson, for their help during cruises We8506a and TT-196. Additionally, I would like to thank Dr. Kristin Rohr of the Pacific Geoscience Centre for the following: a preprint of her Geology article; permission to reproduce some of the data from that article prior to its publication; and for many beneficial discussions about the data and processing in this thesis. This research was funded by the Office of Naval Research.

Chapter 1

Introduction

Geologic processes at mid-ocean ridge crests are an important research topic in marine geology. Magmatic, thermal, and mechanical processes are among those of interest. These processes are not fully understood, but have a direct influence on the generation and evolution of oceanic crust. In particular, the geologic structure of oceanic crust will be directly affected by these processes. Consequently, a knowledge of crustal structure at ridge crests can lend insight into the nature of these processes. The presence or absence of magma chambers is a specific example of a question which can be addressed with structural data. Another example is the relation between oceanic crust and ophiolite complexes. Such questions form the basis of the research in this thesis.

The standard method of determining oceanic crustal structure is through the use of marine seismic reflection techniques. Acoustic energy propagating vertically in the crust will be reflected from interfaces where there are marked changes in composition or other physical properties (such as porosity). These changes represent the large scale structural features of interest. Ridge crests are nearly two dimensional, with the structure varying perpendicular to the strike of the ridge and being roughly constant parallel to the strike. Linear reflection profiles perpendicular to the ridge crest are thus well suited to the problem of determining crustal structure. Resolution is an important concern in seismic reflection surveys. In

order to provide high resolution reflection data it was decided to use the University of Washington's Deep Towed Seismic Reflection System. This system employs a hybrid reflection geometry in which the hydrophone array is towed very close to the sea floor. A more detailed description of this system and its advantages can be found in the next chapter.

Where to obtain the seismic data needed to address the structural questions presented above? The Juan de Fuca (JDF) ridge off the coast of Washington and Oregon (Figure 1) was chosen for two reasons. Convenience is the first reason. The JDF is relatively close to the west coast of North America, and is therefore close to several marine research facilities. Completeness or continuity is the second reason. A large amount of research has already been conducted on the JDF, including; high resolution mapping; dredging and submersible programs; geochemical sampling; photographic, magnetic, and gravity surveys; and previous seismic work. This body of data was useful in planning the reflection surveys, and also aided in the interpretation of the results.

The JDF is a medium rate spreading center with a total opening rate of 6 cm/yr [Atwater, 1970]. It strikes approximately N 20°E and is roughly 450 km long. The JDF forms part of the boundary between the Pacific plate on the west and the Juan de Fuca plate on the east (Figure 1). The ridge is bounded on the north by the Sovanco Fracture Zone and on the south by the Blanco Fracture Zone. On the JDF there are smaller offsets, of which the Cobb Offset is the largest. Average

Figure 1. Location map showing the major tectonic features of the northeast Pacific, including some of the larger segments of the Juan de Fuca Ridge. The areas in the boxes labeled A and B are shown in more detail in Figures 3 and 6, respectively.

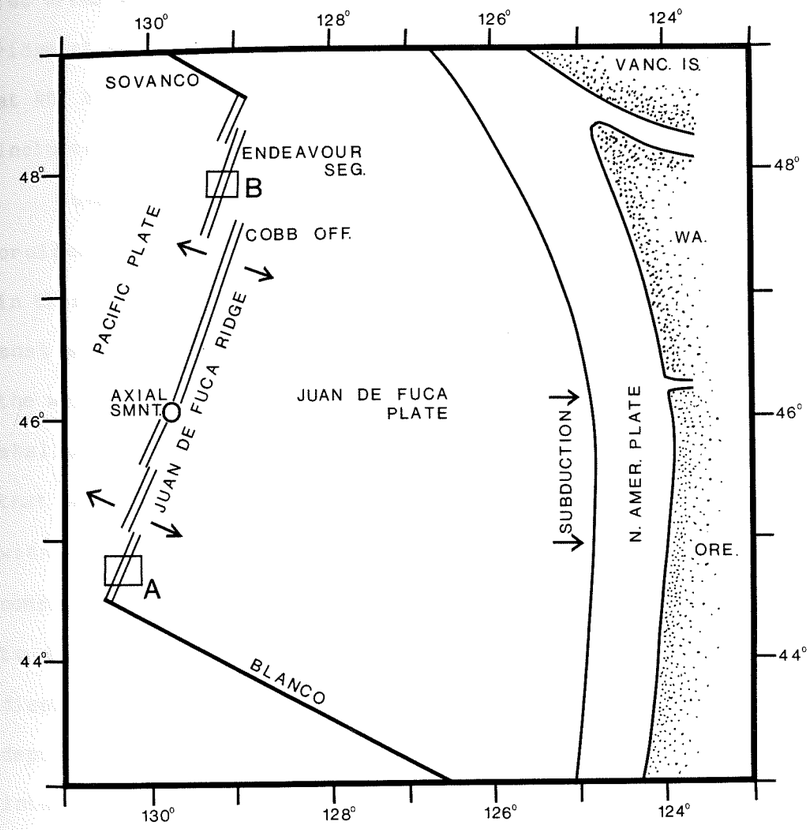

water depth at the ridge crest is roughly 2200 meters and the ridge stands on the order of 500 meters above the surrounding abyssal plain. Two areas were chosen for profiling, one on southern portion of the ridge at 44° 45' N latitude, and one on the northern part of the ridge at 48° N latitude. A detailed description of the survey areas is included in the next chapter.

Several profiles were made in each area over the course of two cruises. Six processed profiles, three from each area, are presented in this thesis. The profiles all show very similar structure. The most striking features are the relatively transparent upper crust and the well layered lower crust. Very few coherent reflectors are seen shallower than approximately 3.5 km in the crust. The crust below that depth displays considerable layering. This structure agrees well with models of oceanic crust developed from studies of ophiolite complexes. The layering correlates with the transition from isotropic to layered gabbros. One of the profiles from the southern area displays a reflector centered beneath the axis of the ridge crest at a depth of roughly 3 kilometers. On account of its position it could be interpreted as a reflection off the roof of a magma chamber. Attempts to verify this interpretation by examining the polarity of the reflection failed, as no definite polarity reversal could be discerned. Instead, the profiles are interpreted as showing no evidence of steady-state magma chambers, an interpretation which is based on seismic refraction data. A final conclusion that can be

drawn is that deep towed seismic reflection techniques are capable of resolving crustal structure at mid-ocean ridges.

Chapter 2 of this thesis describes the survey areas and the data collection. Chapter 3 covers the processing of the data. The results and preliminary discussion are contained in chapter 4. In chapter 5 interpretations are made and supported, and in chapter 6 a brief summary is presented.

Chapter 2

Data Collection

The seismic reflection data in this thesis are from two areas on the Juan de Fuca Ridge (JDF) (Figure 1). Area A is located at the southern end at 44° 45' N latitude, near the intersection of the ridge with the Blanco Fracture Zone. Area B is farther north on the ridge at a latitude of 48° N. Area A was visited on cruise We8506a of the R/V Wecoma in June of 1985. Both Area A and Area B were visited on cruise TT-196 of the R/V Thomas G. Thompson in April of 1986. This chapter describes the profiling system used, gives detailed descriptions of the survey areas, and covers the specifics of the data collection. After the description of the University of Washington Deep Towed Seismic Reflection System, the other information will be presented in the chronological context of the two cruises.

Horizontal resolution is a primary consideration in seismic reflection profiling. In the deep waters of the survey areas this can be a significant problem for conventional profiling systems employing surface sources and receivers. The problem arises from the fact that a surface streamer can receive coherent energy from a large area of the ocean floor, thus averaging out details. The larger the area, the poorer the resolution. Reducing the amount of averaging is the key to the increased resolution of the University of Washington's Deep Towed Seismic Reflection System (hereafter referred to as Deep Tow). The Deep Tow uses a hybrid reflection geometry to achieve lower averaging. Instead of a surface towed streamer, the Deep Tow uses a streamer

towed within a few hundred meters of the ocean floor. Deep Tow and traditional systems are compared in Figure 2. Bowen [1984] has shown that deep towed reflection streamers can offer on the order of an 70% reduction in the area of sea floor, and more importantly the area of sub-bottom, that is averaged.

The main components of the Deep Tow are the hydrophone streamer, the remote electronics package, and the shipboard electronics. The hydrophone streamer consists of 20 hydrophones enclosed in an oil filled plastic housing. Mineral oil is used to compensate for pressure and keep the streamer from collapsing. The 20 hydrophones are summed to provide one signal. This improves the signal to noise ratio of the streamer. Furthermore, the 1.5 m spacing between individual hydrophones was chosen so that the directional properties of the streamer attenuate horizontally travelling energy. This energy originates largely from diffractions and side scattering, and is undesirable.

Analog pressure data from the hydrophones passes through a pre-amplifier at the head of the streamer, and then into the Deep Tow's remote electronics package. This package, or "fish", is encased in a stainless steel pressure housing. The primary purpose of the electronics is to digitize the data and prepare it for telemetry to the ship. Power for the electronics reaches the fish via a co-axial tow cable. Data telemetry is accomplished via the same avenue.

The shipboard electronics consists principally of a power supply, equipment for decoding the telemetered data, and a tape drive for

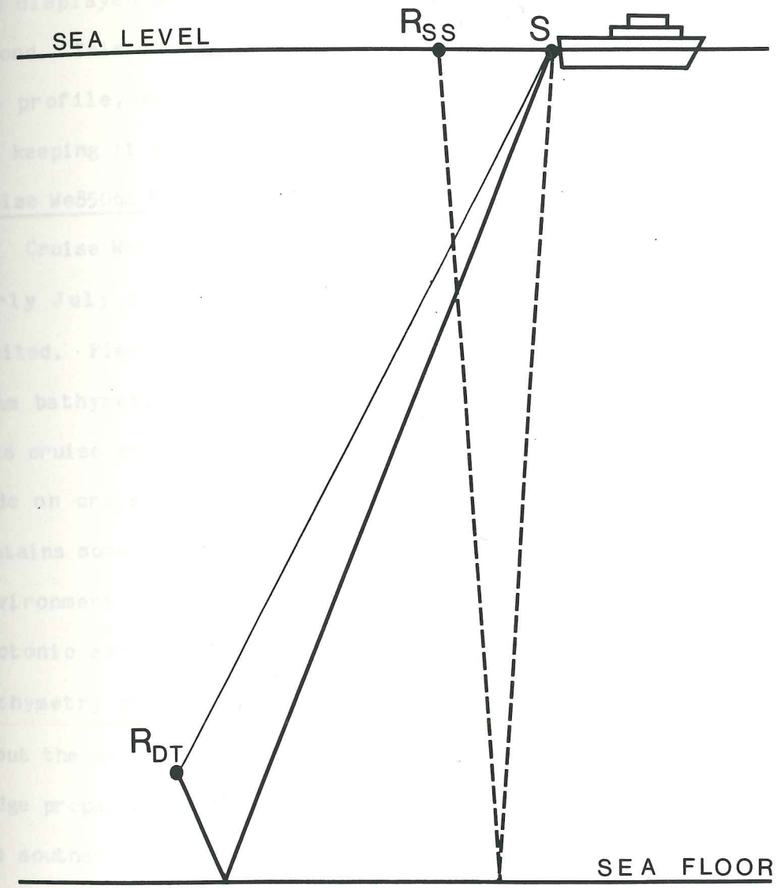

Figure 2. Comparison of surface and deep towed reflection geometries. S is the seismic source. R_{SS} is the surface receiver. R_{DT} is the Deep Tow receiver. The horizonital offset of the surface receiver from the source has been exaggerated for clarity; otherwise the figure is to scale. The dashed line represents the sea floor reflection path for the surface geometry. The heavy solid line indicates the sea floor reflection path for the Deep Tow; the lighter solid line represents the direct water wave path for the Deep Tow. The advantage of the Deep Tow is that the amount of sea floor (and sub-bottom) that is averaged is greatly reduced.

storage of the data. In addition to storing the raw digital data on magnetic tape, it is also passed through a digital to analog converter and displayed on a flat-bed recorder to produce a shipboard monitor record. This display is important not only as a shipboard record of the profile, but is also useful for navigating or "flying" the fish and keeping it a safe distance off the bottom.

Cruise We8506a Data

Cruise We8506a of the R/V Wecoma occurred during late June and early July of 1985. During this cruise Area A of Figure 1 was visited. Figure 3 is an enlargement of this area on a base map of Sea Beam bathymetry. The track lines of two reflection profiles made on this cruise are also shown, as well as the track line of a profile made on cruise TT-196 (which will be described later). Figure 3 also contains some geologic data. This part of the JDF makes an ideal environment for studying ridge crest processes because of its simple tectonic setting. Unlike the central third of the ridge, the bathymetry and magnetic anomalies of the southern JDF are symmetric about the axis of the ridge crest, and have not been influenced by ridge propagation effects [Delaney et al., 1981; Wilson et al., 1984]. The southern JDF exhibits a broad axial high, shoaling to within 2100 meters of sea level. There is a well defined, fault bounded axial valley of 100 meter depth and 1.5 kilometer width [U.S. Geological Survey Juan de Fuca Study Group, 1986]. Centered along the floor of the axial valley is a small cleft roughly 40 meters wide and 20 meters deep [Normark et al., 1987]. This cleft is the locus of volcanic

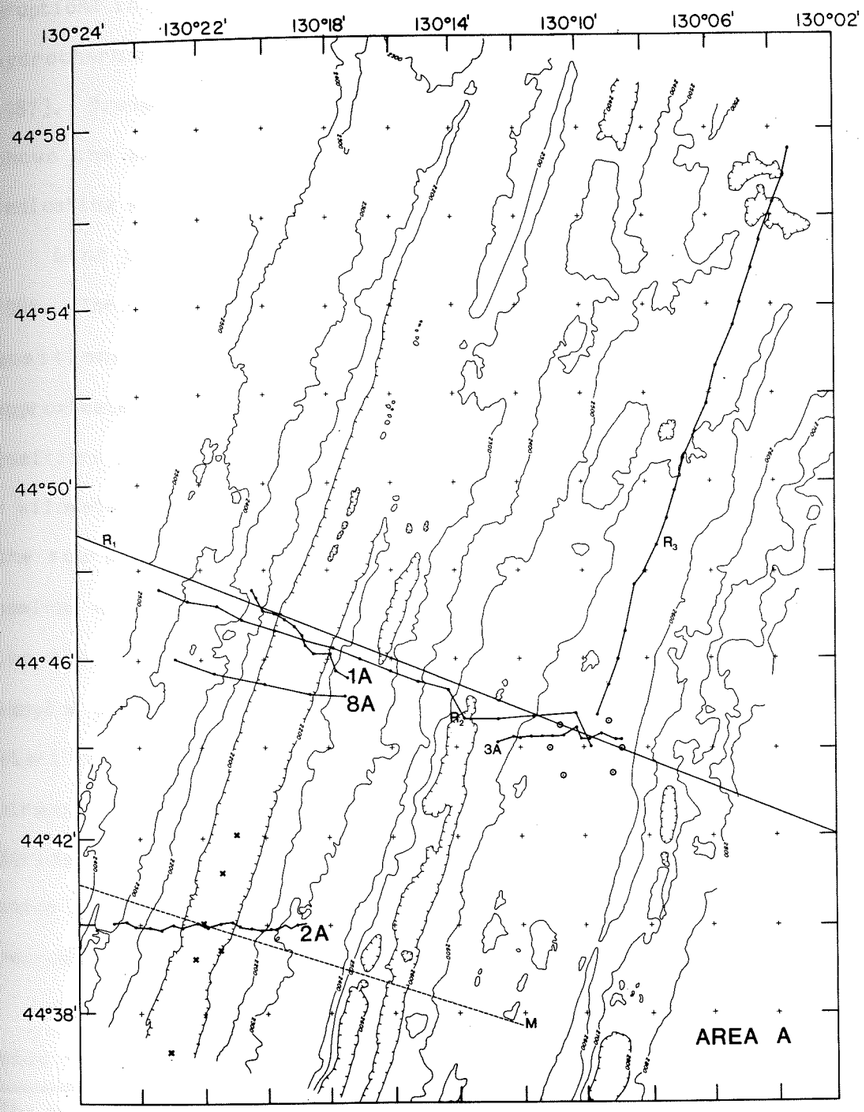

Figure 3. Detail map of Area A on the southern Juan de Fuca. Bathymetry contours are in meters. Lines 1A, 2A, and 8A are the track lines of airgun profiles that are presented in this thesis. Line 3A is the track line of a watergun profile that was not processed. R_1, R_2, and R_3 are refraction lines. The dashed line labeled with an M is the track line of the multichannel profile of Morton et al. [1987], which is discussed in the text. The small X's in the axial valley represent the location of hydrothermal vents.

eruptions in the axial valley, and is the almost exclusive site of hydrothermal venting on the ridge crest in this area [Normark et al., 1987]. Dredge work [Delaney et al., 1981; Dixon et al., 1986] has shown the axial valley to be floored by fresh, glassy ferrobasalt, indicating eruption within the last 2000-5000 years.

Line 1A (see Figure 3 for track line) was profiled on June 26, 1985. The navigation points plotted on Figure 3 are Loran-C ship positions. The line was shot while steaming west at a speed of approximately 1.5 knots. Owing to the towing geometry, the actual positions of the fish and streamer lag the ship's positions by roughly 1 kilometer. A single 4.9 liter (300 cubic inch) airgun was used as the source. It was fired on a 10 second shot schedule, and at a nominal air pressure of 2000 pounds per square inch. 5.12 seconds of the raw digital hydrophone data, sampled in the fish at a rate of 800 samples per second, were recorded on nine-track magnetic tape. The start of the recording window was conincident with the firing of the airgun. 915 shots were recorded; two small segments of data were lost during tape changes. The length of the profile is 6.1 kilometers, which corresponds to a of spacing of 6.7 meters between shots. A reproduction of the shipboard monitor record can be found in Figure 4.

Line 2A (Figure 3) was shot on June 29, 1985. This line was also shot from east to west, and ship navigation also done with Loran-C. The source and shot schedule were the same as Line 1A, but a problem with the air compressor required it to be shut down temporarily. This led to the air gun pressure dropping to 1200 pounds per square inch

Figure 4. Shipboard monitor record for Line 1A. The relatively flat feature at approximately 1.5 seconds two-way travel time is the direct water wave. The irregular feature at 1.7 - 1.8 seconds is the sea floor reflection. Multiples appear at 4.3 - 4.4 seconds. The 0 distance point is the approximate location of the center of the axial valley. Note the strong diffractions off topography. The vertical dashed lines are high-amlitude, low-frequency noise due to cable strum and ship heave.

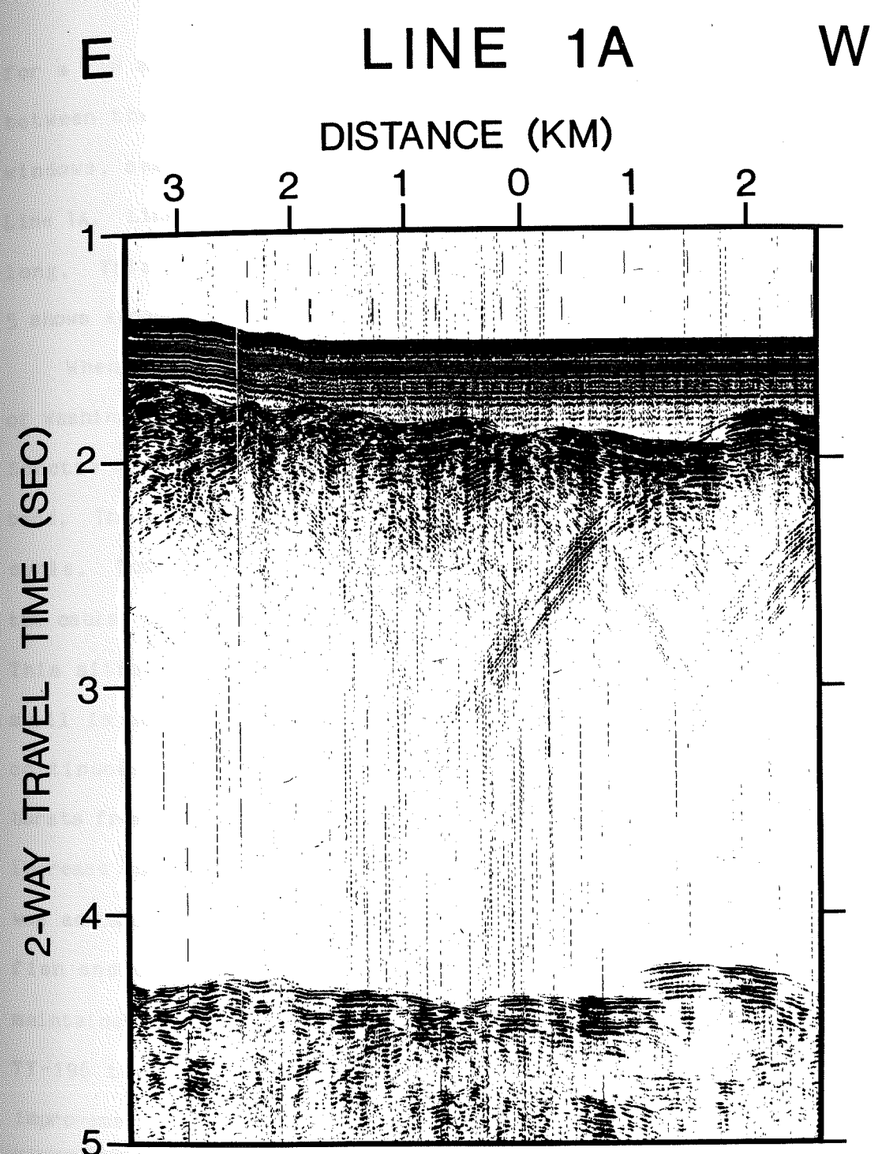

for a few minutes part way through the line. The horizontal offset between the ship and the streamer was 1.1 kilometers, but data windows, sampling, and recording for Line 2A are all the same as for Line 1A. Line 2A also consists of 915 shots, and was 5.8 kilometers long. This gives a shot spacing of 6.3 meters between shots. Figure 5 shows a copy of the shipboard monitor record for Line 2A.

When Line 1A & 2A data was initially analyzed at the University of Washington, a problem with low frequency noise was discovered. Spectra of the data were found to be dominated by noise in the 0-8 Hz band. The probable source of this noise was "cable strum" in the tow cable. Towing a long cable, such as the roughly two kilometer long tow cable, through the water will excite vibrations in the cable. This situation is exacerbated when the heaving of the ship due to swell is added. The data from the Lines 1A & 2A showed a fairly continuous signal from cable strum, and occasionally large noise bursts from ship heave. To remedy this problem, it was decided to increase the mechanical isolation of the streamer from the fish. This was accomplished by inserting a length of elastic cord between the fish and the front end of the streamer. Electrical continuity was maintained by suspending a cable from the elastic cord. During cruise TT-196 the following spring, this modification provided a substantial improvement in signal to noise ratios at low frequencies.

Cruise TT-196 Data

Cruise TT-196 of the R/V Thomas G. Thompson took place during April of 1986. On this cruise, Area B of Figure 1 was visited. Area

Figure 5. Shipboard monitor record for Line 2A. The direct water wave, sea floor reflection and multiple are in roughly the same positions as in Figure 4. 0 distance is the center of the axial valley. Diffractions are less obvious on this profile as compared to those in Figure 4, but the low-frequency noise is worse.

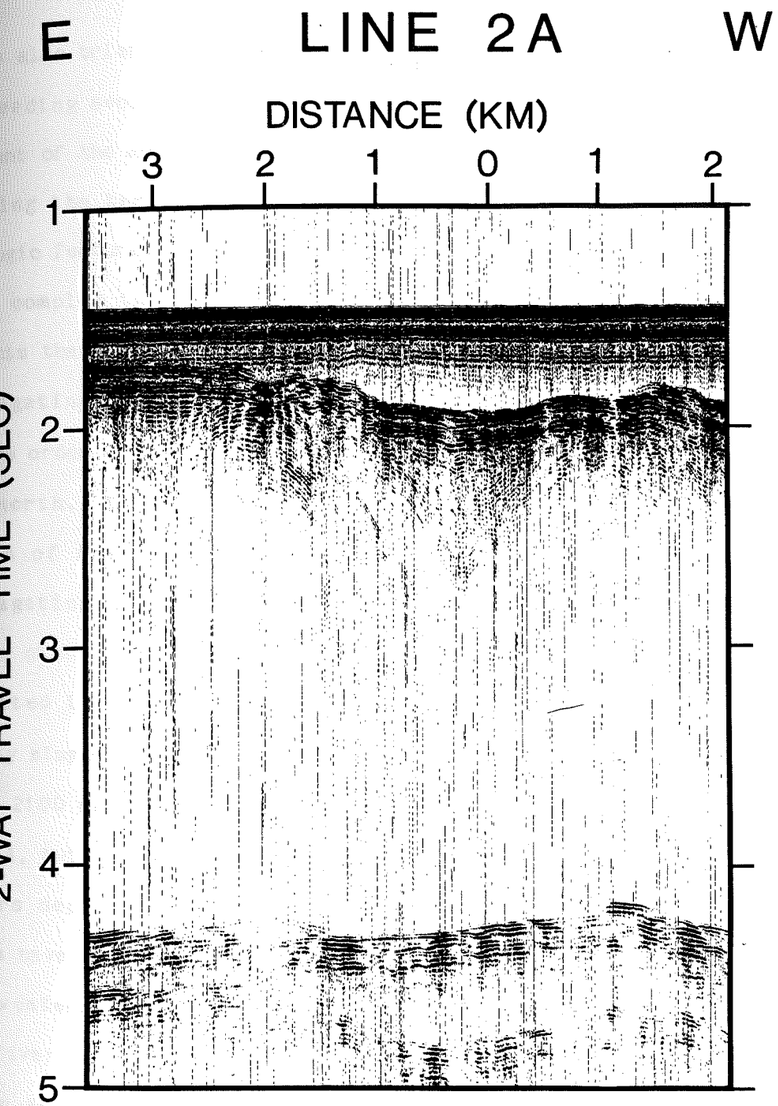

A was also briefly revisited (for a description of Area A, see the preceeding section). Area B is on the southern part of the Endeavour Segment of the JDF. Figure 6 is an enlarged Sea Beam map of Area B, showing the three reflection track lines from this area, and some geologic features. Regionally, this part of the JDF is tectonically more complex than at Area A. Most of the complexity stems from the effects that propagating rifts have had. Wilson et al. [1984] discuss propagating rifts on the JDF in considerable detail. In their model, on the order of 3.0 million years ago, a rift passed by Area B on the way north. The present-day Cobb Offset, roughly 10 kilometers to the south of Area B, is a younger northwards propagating rift. Propagating rifts have the effect of disturbing the ideal symmetry of ridge crest structures. However, Area B has not been directly affected in roughly 3.0 million years, and the near axis structure is fairly simple. In Area B the ridge crest shoals to a depth of less than 2100 meters. The general morphology is also an axial high as in Area A, but not as broad. There is an axial valley of roughly 100 meters depth, and approximately 1.5 kilometer width. Submersible dives have revealed active hydrothermal venting, particularly along the western side of the axial valley, which is fault bounded [Delaney and Tivey, 1988]. Basalt from the floor of the axial valley is not as fresh as that from Area A, and no small cleft is found bisecting the axial valley.

Line 1B (see Figure 6 for track line) was profiled on April 3, 1986. Navigation was recorded with Loran-C. This line was shot with

Figure 6. Detail map of Area B on the Endeavour Segment. Bathymetry in meters. 1B, 3B, and 4B are the track lines of three airgun profiles presented in this thesis. Line 2B is an unprocessed airgun profile, and Line 5B is an unprocessed watergun profile. The dashed line M is the track line of the multichannel line of Rohr et al., which is discussed in the text. The small X's in the axial valley are the locations of hydrothermal vents.

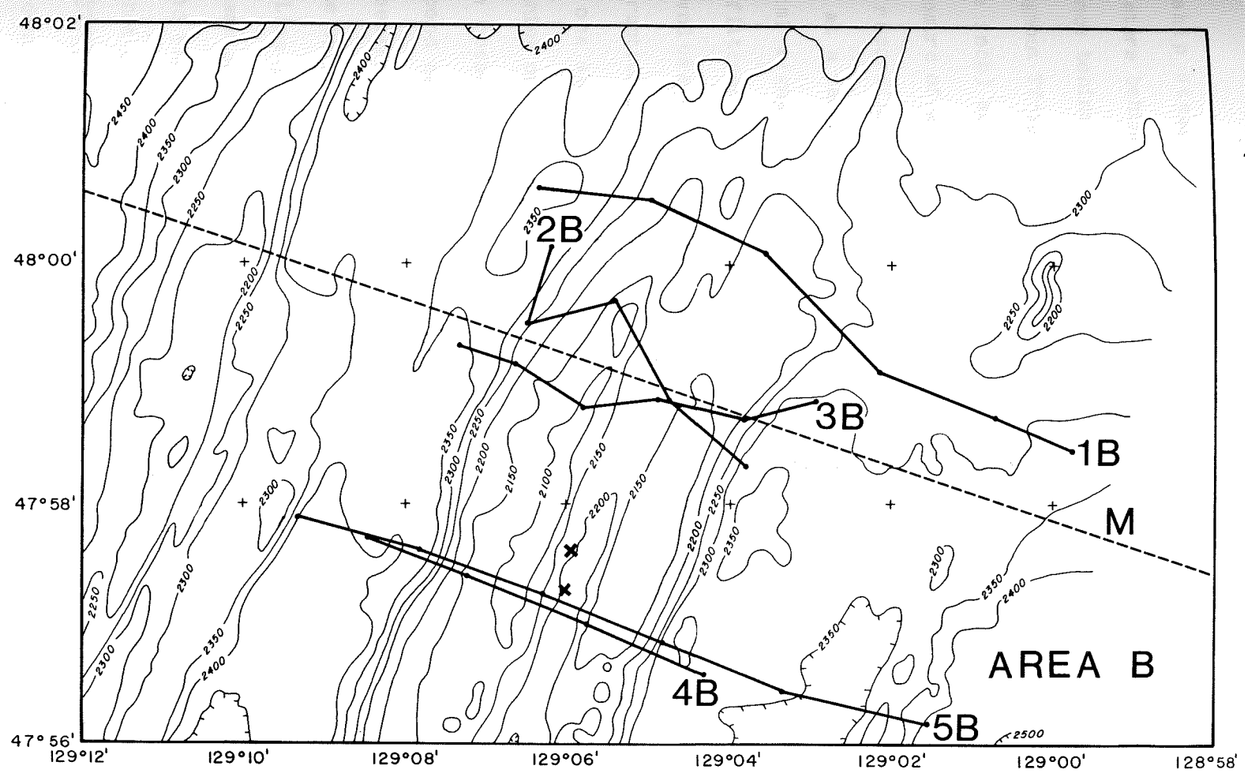

the ship steaming to the west. On this line, the fish was 1.2 kilometers behind the ship, so that fish positions are offset that distance behind (to the east of) the ship positions shown in Figure 6. Throughout TT-196, the seismic source consisted of two 4.9 liter (300 cubic inch) airguns. The guns were fired on an 11 second schedule at a pressure of 2000 pounds per square inch. On this cruise a different data recording scheme was used. Digital data from the fish was the same, at a sample rate of 800 samples per second. On the ship, this digital signal was converted back to an analog signal and then low pass filtered and subsampled. The rationale behind this was to reduce the volume of data to be stored on tape. This eliminated the interruption of data acquisition for changing magnetic tapes. On Line 1B a one second delay was introduced between the airgun shots and the beginning of the data window, which further reduced the volume of data to be recorded. 920 shots consisting of 4 seconds of data (after the 1 second delay) were recorded for this line. Line 1B is 9.5 kilometers long, which gives a shot spacing of 10.3 meters. Figure 7 is the shipboard monitor record for this line.

Line 3B (see Figure 6) was shot on April 3, 1986. Navigation was the same as for Line 1B, only with a horizontal offset of the fish behind the ship of .7 kilometers (the fish to the east). The source and shot schedule were also the same, although one of the airguns was not working for the first two thirds of the profile. Data recording was identical, including the 1 second delay after the shot. On this line, 1500 shots were recorded. The length of Line 3B is 5.8

Figure 7. Shipboard monitor record for Line 1B. The 0 distance point is at the center of the axial valley. Direct water wave, sea floor, and multiple are all as in Figure 4. The regular vertical dashed lines represent timing marks, and are not low-frequency noise.

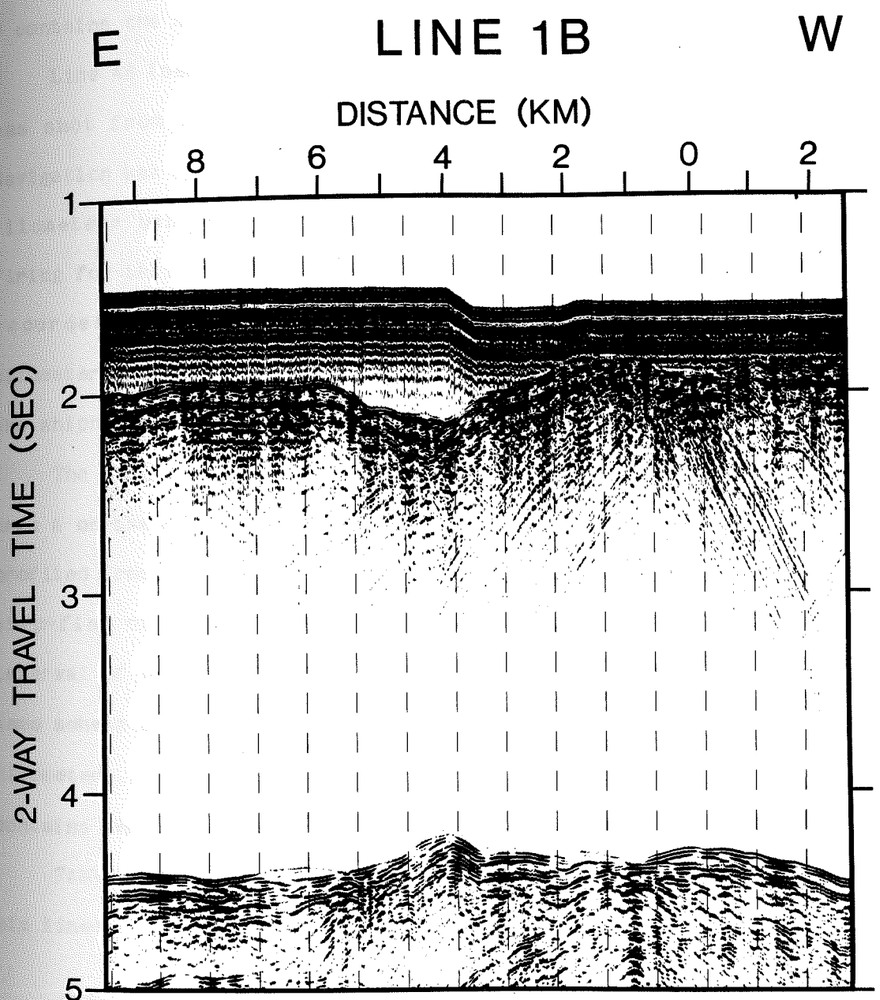

kilometers, which gives a spacing of 3.9 meters between shots. Figure 8 contains the shipboard monitor record for Line 3B.

Line 4B (see Figure 6) was recorded on April 4, 1986. This line was shot from west to east, but has been reversed during processing. Navigation was by Loran-C, and for this line, the fish trailed 1.1 kilometers behind or to the west of the ship. Both airguns were firing for this line at an interval of 11 seconds. 736 shots were recorded with the same scheme as Lines 1B & 3B. Line 4B is 4.5 kilometers long, which corresponds to a shot spacing of 6.1 meters; the shipboard monitor record can be seen in Figure 9.

The final profile in this thesis was recorded on April 6, 1986 in Area A on the southern JDF (see Figure 3 for track line). Line 8A was profiled from east to west, with Loran-C navigation, and a horizontal ship-fish offset of 1 kilometer. Both airguns were firing at an interval of 11 seconds. 1180 shots of data were recorded with the same scheme as the previous three lines. The length of Line 8A is 6.7 kilometers, for a spacing of 5.7 meters between shots. Figure 10 contains the shipboard monitor record for Line 8A.

Table 1 provides a summary of data collection parameters for all six lines.

Figure 8. Shipboard monitor record for Line 3B. 0 distance is the middle of the axial valley. Direct water wave, sea floor, and multiple are all as in Figure 4. Vertical dashes are timing marks.

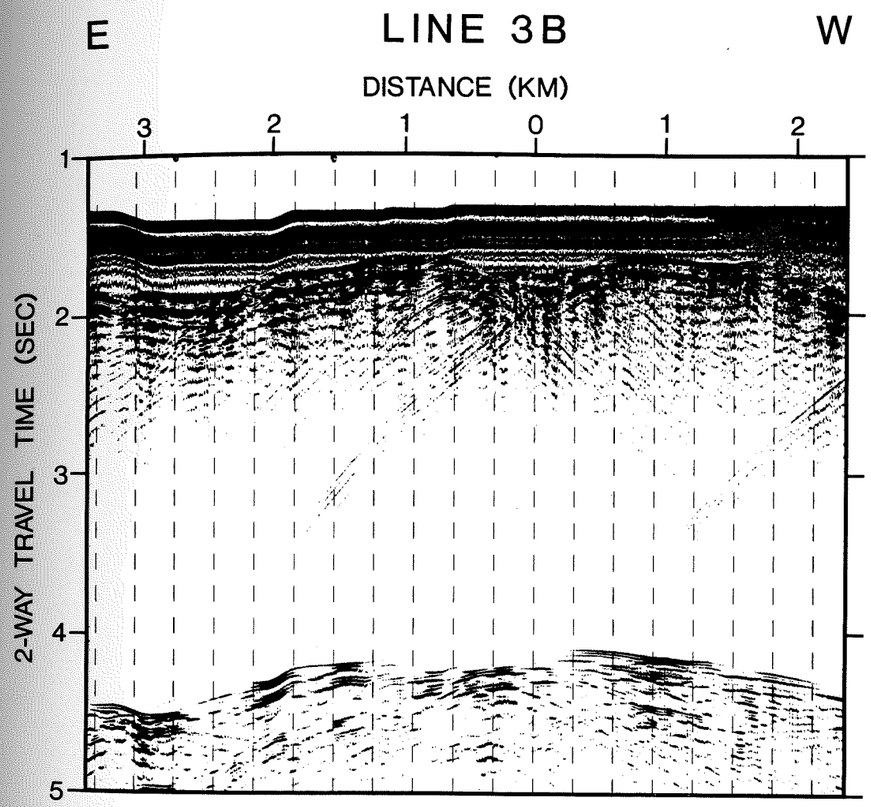

Figure 9. Shipboard monitor record for Line 4B. 0 distance is at the center of the axial valley. Direct water wave, sea floor and multiple as in Figure 4. Vertical dashes are timing marks. Arrows along the bottom border indicate the position of the shots shown at a larger scale in Figure 11.

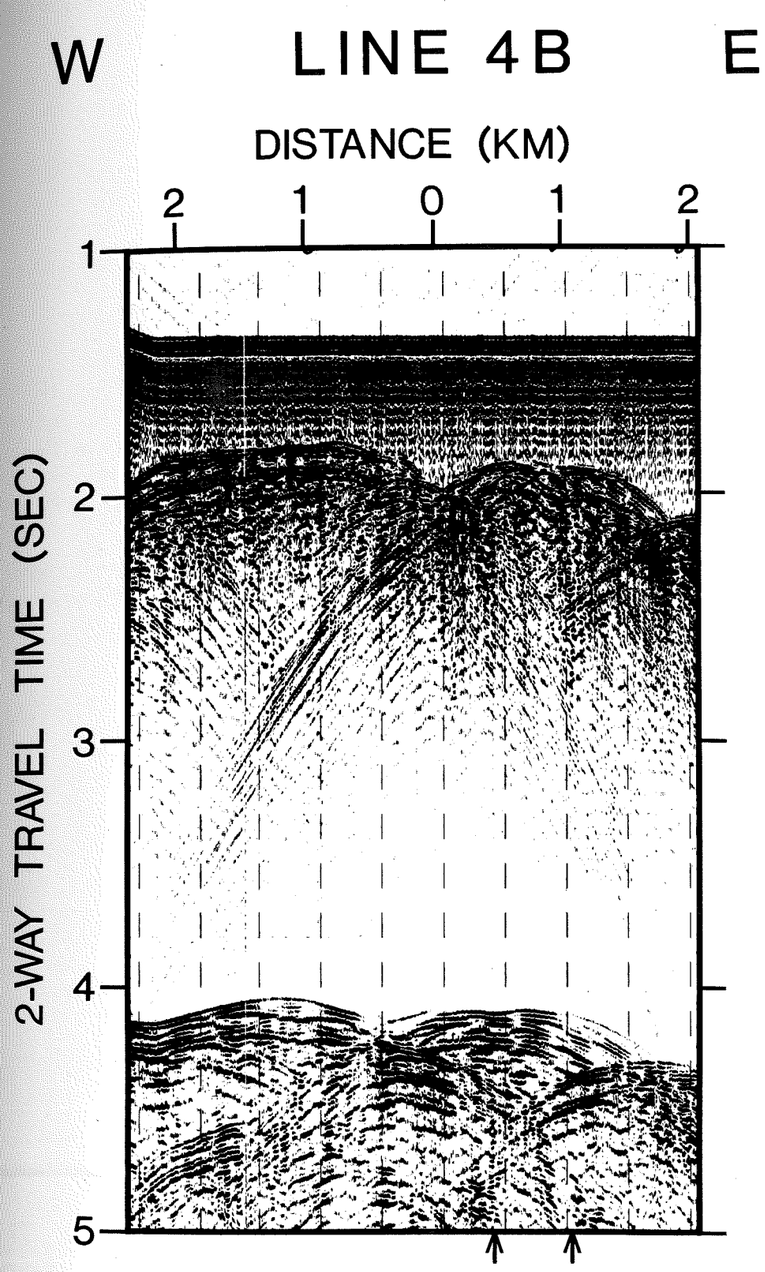

Figure 10. Shipboard monitor record for Line 8A. 0 distance is the approximate location of the center of the axial valley. The direct water wave arrives at a two-way travel time of roughly 1.4 seconds; the sea floor reflection is hard to make out, but arrives at roughly 2.0 seconds. The multiple stands out clearly at roughly 4.2 seconds. Vertical dashes are timing marks; the vertical smears are points at which the paper stuck on the flat-bed recorder.

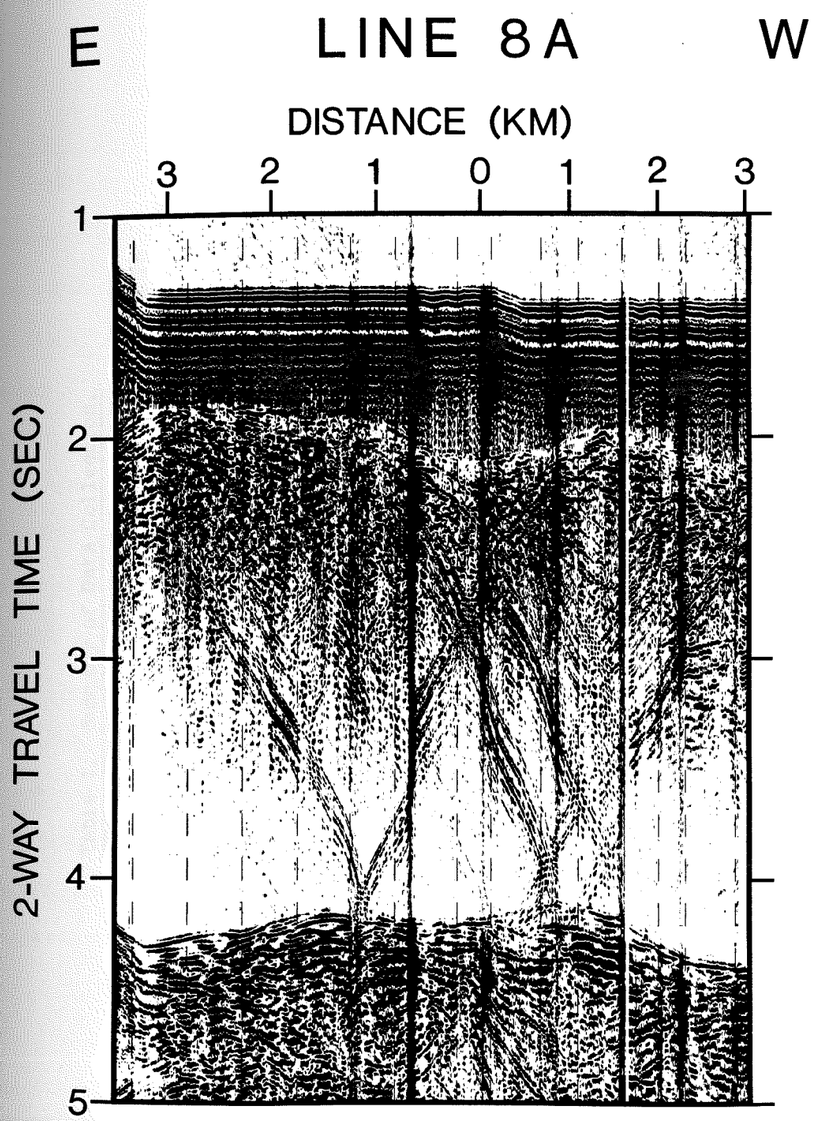

Table 1. Summary of Data Collection.

LINE	CRUISE	AREA	SOURCE[1]	SHOT INTERVAL (sec)	FINAL SAMPLING RATE (sam/sec)	DELAY (sec)	DATA WINDOW LENGTH (sec)	# OF SHOTS	LENGTH OF LINE (km)	SHOT SPACING (meters)	NOTES
1A	We8506a	A	1	10	800	0	5.12	915	6.1	6.7	
2A	We8506a	A	1	10	800	0	5.12	915	5.8	6.3	2
1B	TT-196	B	2	11	100	1	4.00	920	9.5	10.3	
3B	TT-196	B	2	11	100	1	4.00	1500	5.8	3.9	3
4B	TT-196	B	2	11	100	1	4.00	736	4.5	6.1	4
8A	TT-196	A	2	11	100	1	4.00	1180	6.7	5.7	

NOTES: 1. Number of 4.9 liter (300 cubic inch) airguns.
2. Air compressor temporarily out of order; low air pressure for portions of line.
3. Only one airgun functioning for first two-thirds of line.
4. Only line profiled from west to east.
(Loran-C navigation for all lines. For information on experimental geometry, such as horizontal fish-ship offset, see Table 6.)

Chapter 3

Data Processing

Introduction to Data Processing

The shipboard monitor records in Figures 4,5, and 7-10 show that processing is required in order to bring out the deeper crustal structure. In these figures it can be seen that signal strength drops rapidly after the reflections from the ocean floor. There are also strong diffractions off of topographic features which obscure sub-bottom reflections. Additionally, the airgun source signatures contain many low frequency reverberations which last for a substantial period of time. All of these problems, as well as that of noise in the profiled sections, complicate the interpretation of the geologic structure. To reduce the impact of these complications, a number of seismic data processing techniques were applied to the data. A description of these techniques is the purpose of this chapter.

A number of steps were taken in producing the final processed sections. The primary steps were deconvolution, wave equation migration, and automatic gain control. There were also a number of intermediate steps, such as stacking and filtering. To discuss in detail each step as applied to each line would be a considerable undertaking. It is also largely an unnecessary undertaking, since each step is much the same for all lines. Therefore, the bulk of this chapter will consist of a detailed description of the processing of only one line, Line 4B. Such small differences as do exist between the processing of the various other lines will be summarized in tables

at the end of the chapter. Before beginning with the discussion of the processing of Line 4B, an important point should be made. A great deal of experimentation went into deciding which processing techniques to apply, how to apply them, and what order to apply them in. The processing described below gave the clearest final result; some intermediate steps may not have seemed necessary, but were found to be beneficial after later processing.

Processing

A small problem with the data from Line 4B was detected during initial playback of the data. This problem was also found on the other lines collected on cruise TT-196. The onset of the data window was found to be occasionally advanced or delayed by a few samples at random intervals throughout the profile. This caused entire traces to appear shifted by several milliseconds relative to adjacent traces. This problem was easily remedied by catalogging the erroneous shifts in a profile, and then adding a few zeroes or discarding a few samples at the beginning of the traces as necessary. Figure 11a shows 100 shots from Line 4B after this preliminary step was taken. Only 100 shots are shown, as plotting all 736 at the same scale would have resulted in a plot too large to be reproduced here. This portion of the line is from the right hand side of the profile as seen in Figure 9, and is marked along the bottom border of the plot.

The first step in processing was to band pass filter the data to remove noise that was out of the signal band. This required a knowledge of the frequency content of the data. To obtain this

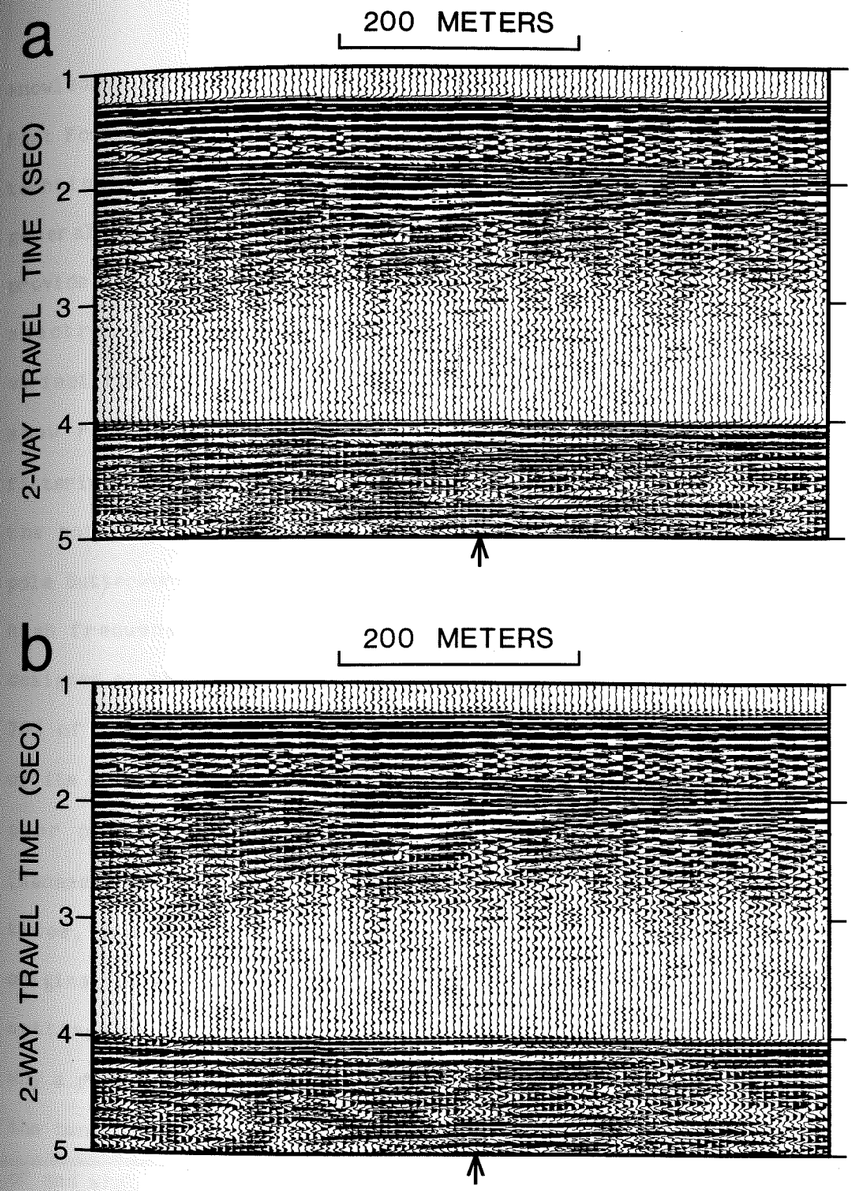

Figure 11. a. 100 shots of raw data from Line 4B (see Figure 9 for position). b. The same 100 shots after filtering. In both panels, the sea floor reflection appears at roughly 1.8 seconds. The arrows on the bottom borders show the location of shots used for the spectra of Figures 12a and 12b.

knowledge, the approach used was to generate line spectra by taking Fast Fourier Transforms of the data [Brigham, 1974]. More complicated techniques could have been used for calculating spectra, but the general features would have been the same. Other techniques would provide information about the reliability of smaller features in the spectra, but this information would be of little use, given the variability of the spectra from shot to shot. Figures 12a and 12b show representative line spectra for the data before and after filtering. The spectra are from the shot indicated with an arrow on the bottom of the plots in Figures 11a and 11b. A time domain, six pole Butterworth band pass filter was used for Line 4B, with low and high frequency settings of 6 and 28 Hz respectively. The filter was designed so that the frequency settings were attenuated 3 dB (cut to 70% of their original value). A Butterworth filter was used because of its flat amplitude response in the pass band. To correct for the poor phase response of the Butterworth, the filter was cascaded [Kanasewich, 1973, p. 199]. This process requires applying the filter twice, and so yields an amplitude response which is the square of the original filter's response (for example the response at the band pass settings would be -6 dB instead of the original -3 dB). This is also why a relatively low number of poles was chosen, so that the flanks of the band pass would not become too steep. Deciding what to filter out of and what to leave in the spectrum was accomplished by filtering a portion of the data with various filter settings and examining the results. A low pass with a cut of 6 Hz left mostly incoherent noise

Figure 12. a. Representative line spectrum for raw data (see Figure 11a for the location of the shot used for the spectrum). b. Line spectrum of the same shot as in 12a, after filtering (see Figure 11b for the location of the shot used for the spectrum). c. Line spectrum of deconvolved, stacked data. The shot used for this spectrum is the stacked shot which includes the raw data shot used for the spectrum in 12a and 12b, and is indicated with an arrow on the bottom Figure 15a. d. Line spectrum of the same shot as in 12c, after filtering. See Figure 15b for location.

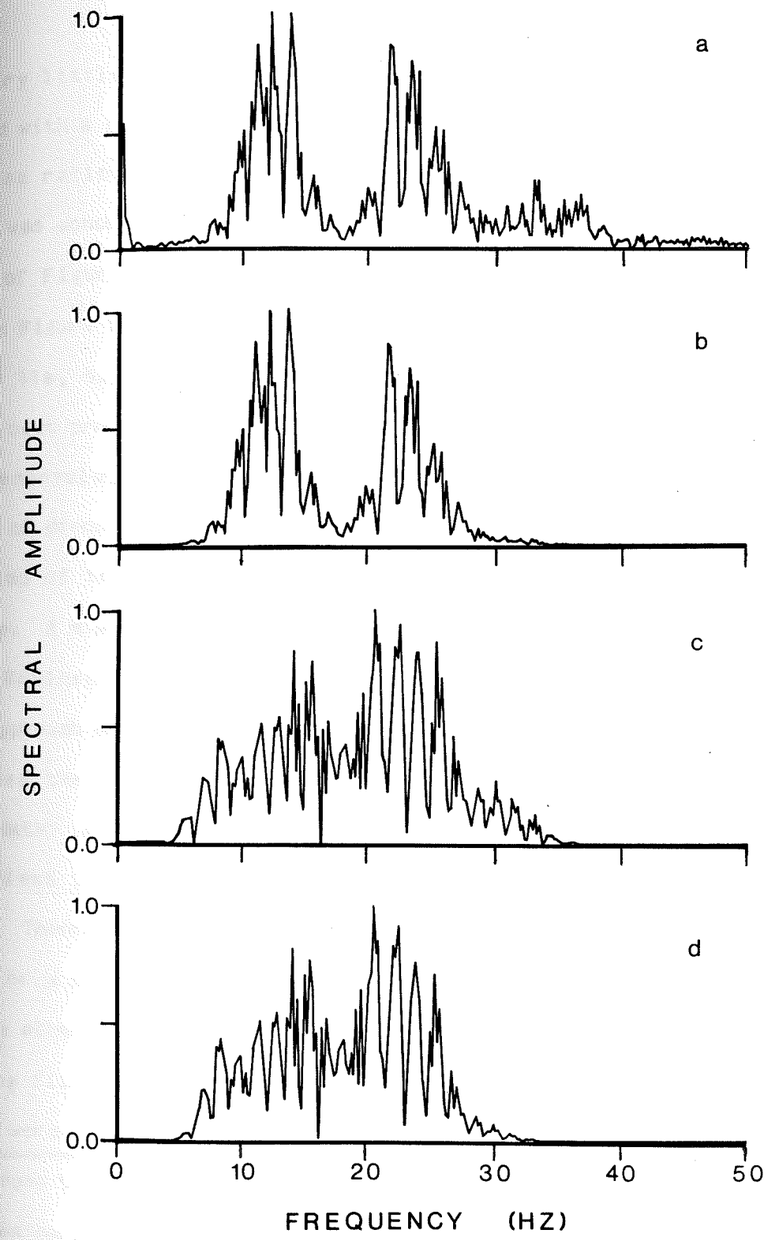

and very little seismic energy. The frequency band above 28 Hz, sampled with a high pass filter, was found to have a very low signal to noise ratio. Similar tests showed that the main band of seismic energy was concentrated between 6 and 28 Hz. Figure 11b shows the 100 shots of Figure 11a after application of the band pass filter. The data in Figure 11b does not appear significantly altered from that in Figure 11a, but this filtering step was found to improve the results of the next processing step.

Deconvolution was the next process applied to the data. The object of deconvolution in seismic processing is to contract the time duration of the seismic pulse and thus improve resolution in the profile. A statistical least squares approach was used [Berkhout, 1977; Robinson and Treitel, 1980, Ch. 6 & 7; Robinson, 1983, Ch. 2]. This approach assumes a convolutional model for the seismic trace, and involves the design of a filter or operator to be convolved with the input data. A new filter is designed for each trace. An important ingredient in the design of the filter is the desired output pulse shape. Theoretically, the optimum output pulse in terms of resolution would be a one sample wide spike, but the process can also be used to produce other output shapes. The former type of filter would be a spiking filter, the latter a wave shaping filter. Both sorts of filter were tested with the data for Line 4B, and wave shaping filters were found to produce the best results. The desired output shape that was used can be seen in Figure 13. There are a number of variables in designing least squares filters. Aside from the desired output, other

Figure 13. The desired output pulse used in designing the wave shaping filters for Lines 3B, 4B, and 8A. After Parkes and Hatton [1986].

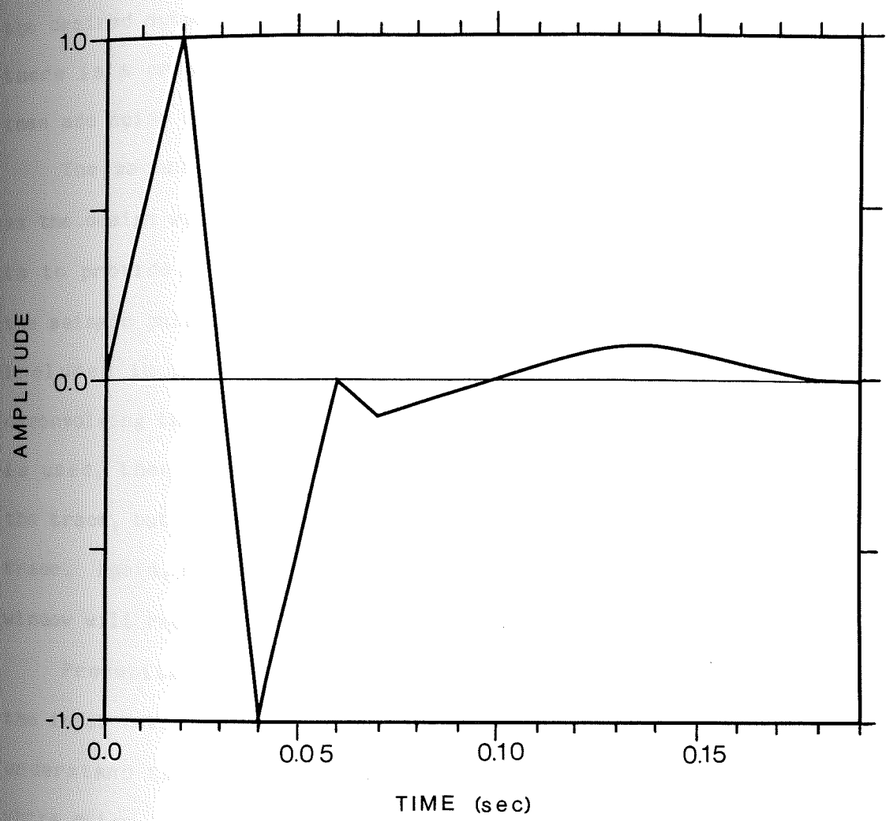

variables are the length of the filter, the amount of input data to be used in designing the filter, the amount of pre-whitening of the data, and the desired position or lag of the output pulse.

Filter length affects the degree to which the filter can match the desired output. Longer filters do a better job of matching, but there is a practical limit beyond which filters will do little more than add noise to the output.

The amount of input data used to design the filter is also known as the design window length. The primary purpose of the design window is to provide information to the design process about the nature of the seismic pulse to be re-shaped. The more of the trace that is included in the design window, the better the filter will be at deconvolving the entire trace. If only a small portion of the trace is used, then the filter will work well when applied to that part of the trace, but will perform poorly when applied to the rest of the trace. Again, however, a practical limit exists; too long of a design window will require a prohibitive amount of calculation.

Pre-whitening involves adding a small quantity of white noise to the input data. This stabilizes the least squares inversion. To understand this, consider the frequency domain equivalent of adding white noise. In the frequency domain, white noise is a DC signal; adding white noise corresponds to boosting all spectral amplitudes by a given amount. This is important where, for example, the spectrum of the seismic signal exhibits a notch. At this frequency noise will predominate, and in the inversion, the noise will be greatly

amplified. Pre-whitening will limit the amplification of noise in bands of poor signal to noise ratio.

Finally, the lag of the desired output also affects the performance of the filter. The filter is applied by convolving it with the data, and the greater the lag, the greater the overlap between the filter and the data. More lag means the filter "sees" more of the data before producing the output. An ideal lag can be determined by experimenting with the data and different values of the lag.

Numerous combinations of the above mentioned variables were experimented with before determining the optimum combination for use on the entire profile for Line 4B. The desired output pulse has already been introduced (Figure 13). The operator length was 200 milliseconds, or 20 samples since the sample rate was 100 samples per second. A 2 second design window was used, which began at the onset of the direct water wave. This window represents a compromise between a window containing as much of the important information about the seismic pulse as possible, and one which is computationally efficient. The amount of pre-whitening used was 1 percent. This means that a constant equal to 1 percent of the peak spectral energy was added to each spectral amplitude. A lag of 20 samples was found to be optimum. Figure 14 shows the 100 shots from Figure 11b after the deconvolution described above.

The next step in processing Line 4B was to "group stack" the data. By this is meant that several successive traces, in this case

Figure 14. The 100 shots of Figure 11 after deconvolution.

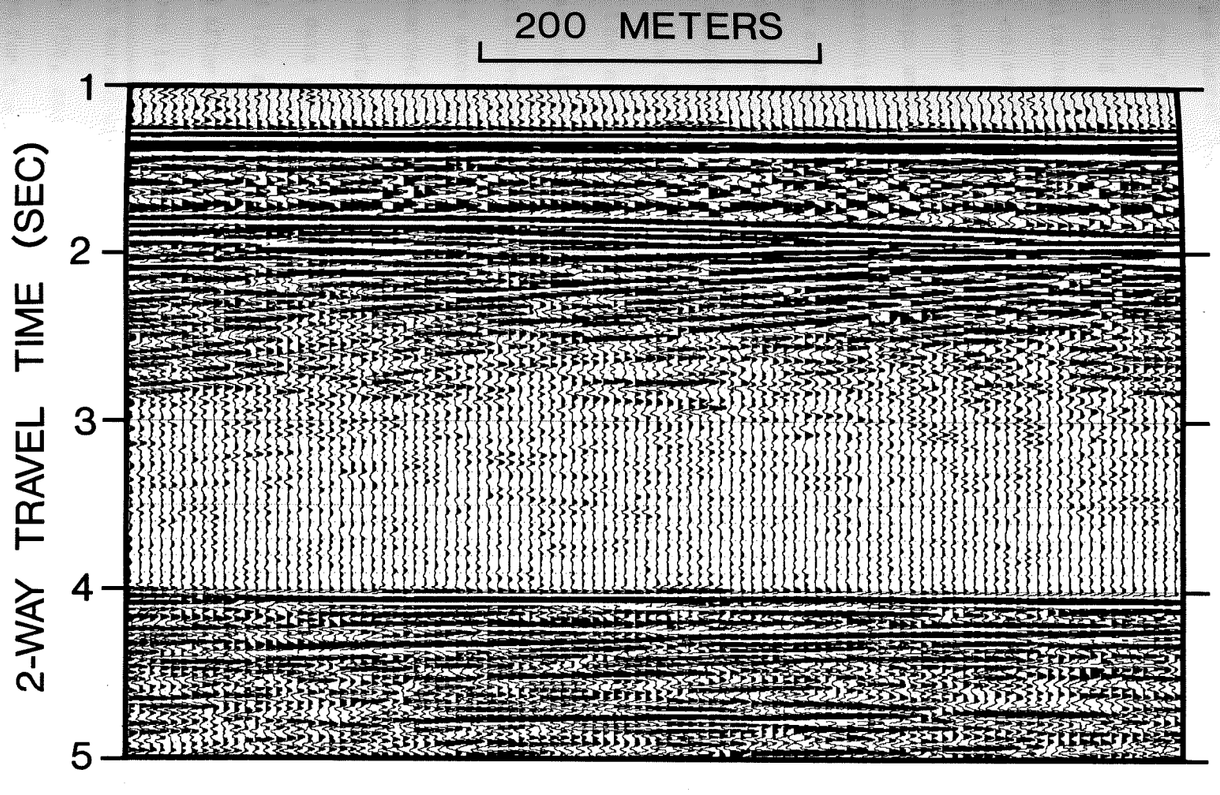

8, are summed together, and the resultant trace amplitudes divided by 8. The reasons this step was applied are two fold. First of all, stacking helps alleviate the problem of in-band noise. The preliminary band pass filtering removed only out-of-band noise, that is, noise that was outside the main band of the seismic signal. Whatever noise was in-band presumably remains after deconvolution, perhaps amplified somewhat, or augmented with spurious noise from the deconvolution itself. Assuming that this in-band noise is Gaussian, then averaging traces should provide, in this case, a factor of $\sqrt{8}$ reduction in noise levels [Hatton et al., 1986]. The second benefit of stacking the data is that it results in a reduction in the amount of data to be processed in subsequent steps. An eight-fold reduction in the amount of data results in a considerable savings in computational time during migration. Conceivably, the amount of data could have been reduced by eliminating records without stacking, but this amounts largely to wasting that portion of the data which is discarded. Figure 15a shows all of Line 4B after stacking.

Before migrating the data, it was found to be useful to filter the data again to remove spurious high frequency noise. Figures 12c and 12d show representative line spectra of the stacked data before and after band pass filtering. The results of this filtering are shown in Figure 15b. The spectra in Figures 12c and 12d are for a shot marked with an arrow at the bottom of the profiles in Figures 15a and 15b, and are for the stacked shot which includes the single shot used for the earlier examples of spectra. The same band pass filter

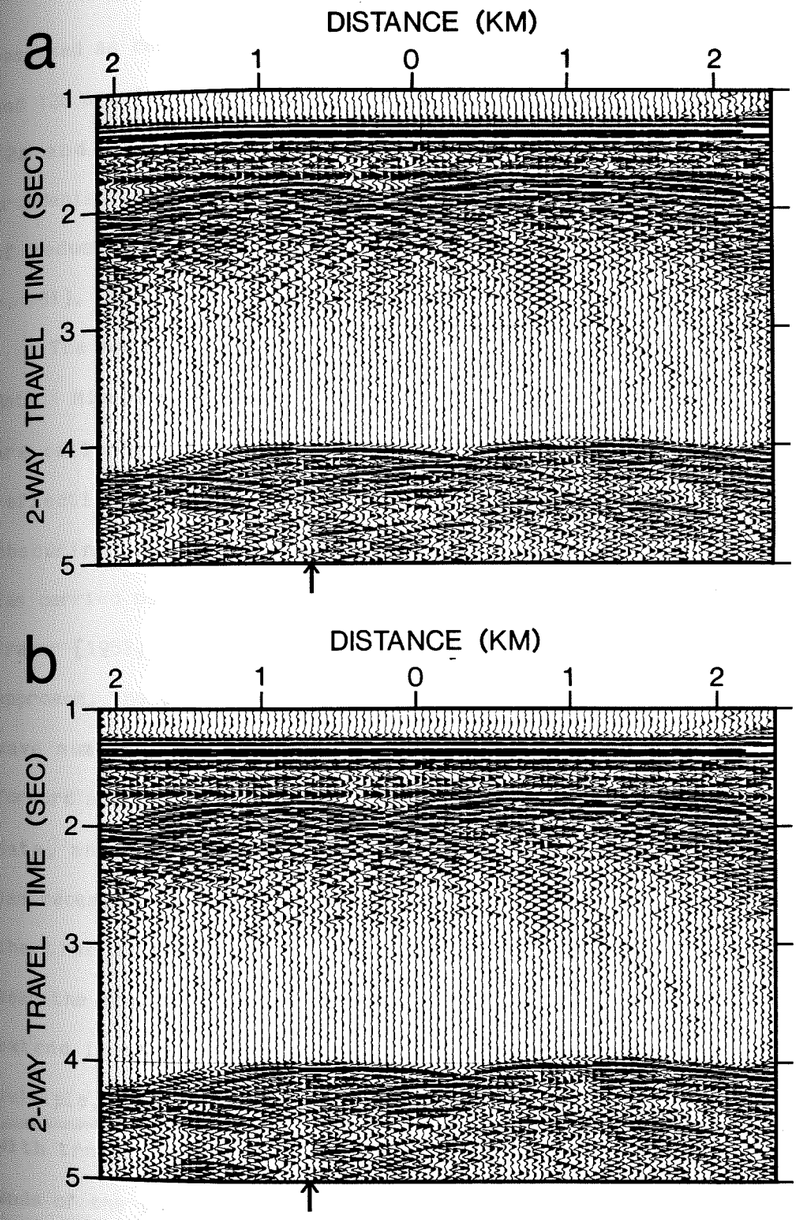

Figure 15. a. Entire profile for Line 4B after deconvolution and stacking. The arrow on the bottom border indicates the postion of the shot used for the line spectrum in Figure 12c. b. The data from a. after filtering (arrow again shows location of shot used for spectrum). In both panels, 0 distance shows the center of the axial valley.

was used as described previously. Although the spectra in Figures 12c and 12d are for stacked data, comparison with the spectra in Figures 12a and 12b shows that the deconvolution has had the effect of broadening the spectral peaks. This corresponds to the desired effect of reducing the time duration of the seismic pulse [Bracewell, 1986, p. 151].

The next major stage in processing Line 4B was to migrate the data. Migration is a process in which hyperbolic diffraction patterns are collapsed to points. These diffractions are generated by side reflections off of topographic features, and have the effect of obscuring sub-bottom features. Wave equation migration of the data was carried out with the frequency-wave number approach of Carter and Frazer [1982; see also Stolt, 1978; Chun and Jacewitz, 1981]. In this approach, the diffraction hyperbolas are collapsed in the frequency-wave number domain through a mapping process. This mapping requires forward and inverse two-dimensional Fast Fourier transforms of the data, and therefore requires some preparatory steps. The preparation was necessary to avoid wrap around problems with the transform. Along the time axis, each trace was tapered to zero at the beginning and near the end, and then zeroes were added at the end of the trace to extend it to 512 samples. The data were tapered at the onset of the multiple, as including all of this feature led to migrated sections with troublesome artifacts. Along the distance axis, traces at the ends of the profile were tapered or progressively muted, and then traces of zeroes were added to extend the total number of records to

256. After this, the data were transformed, and then the frequency-wave number mapping of Carter and Frazer [1982] was applied. Following this, the data were inverse transformed. Figure 16a shows the data after migration with a velocity of 1.5 kilometers per second. The strong diffractions off topography on the sea floor have been removed. Figure 16b shows the data after migration with a velocity of 2.4 kilometers per second. The higher velocity represents a root mean square (rms) velocity for the upper crust, to a depth of approximately 2 kilometers. As Carter and Frazer [1982] point out, migrating with the rms velocity for a given depth will improve the removal of diffractions from features at that depth. There is a trade off in that diffractions at shallow depths will be over-migrated. As the focus of this thesis is overall crustal structure, an intermediate velocity was chosen. Examination of Figure 16a and 16b shows that the higher velocity had little effect on shallow features, but deeper features were enhanced.

To make the data easier to interpret, it was decided to perform a running stack after migration. By running stack is meant that the data traces are smoothed, in this case by three's. For instance, the first output trace would be an average of the first, second and third input traces. The second output trace would be the average of the second, third and fourth input traces, and so on. This has the effect of attenuating incoherent noise, and acts as a crude coherency filter. Figures 17a and 17b show the migrated data of Figure 16a and 16b after application of the running stack.

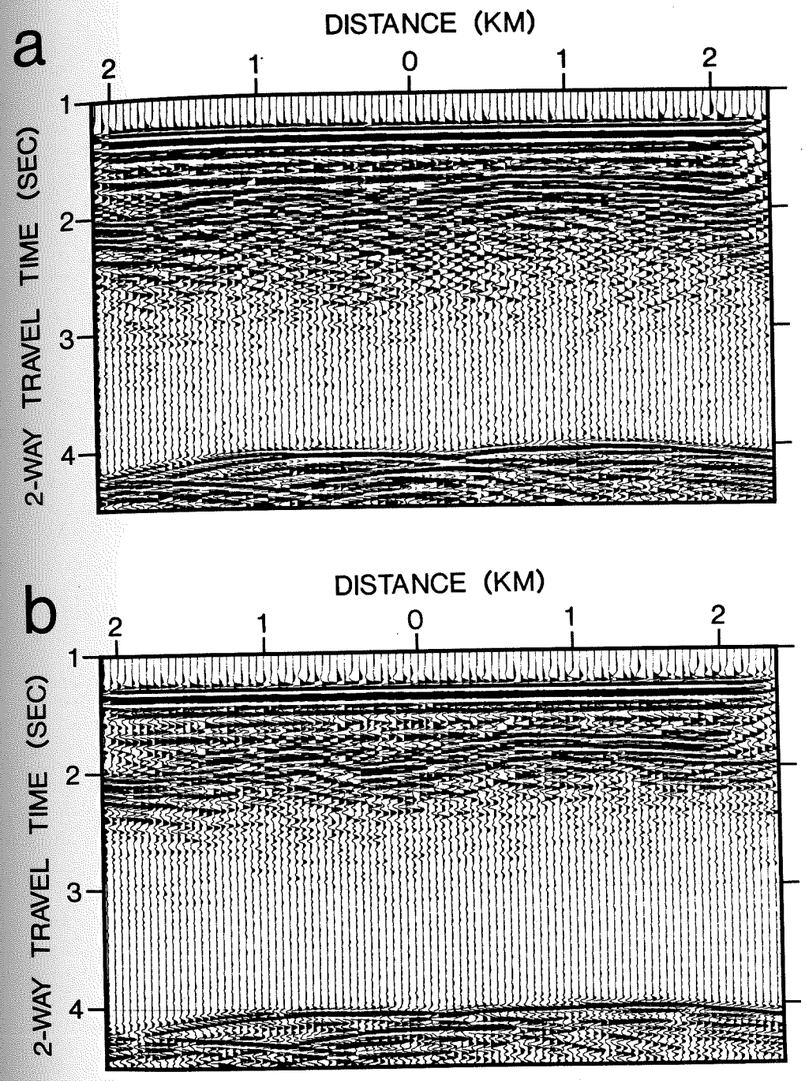

Figure 16. a. Line 4B after migration with a velocity of 1.5 kilometers per second. b. Line 4b after migration with a velocity of 2.4 kilometers per second. Compare with Figure 15b. 0 distance shows approximate location of center of axial valley.

Figure 17. a. Lower migration velocity version of Line 4B after running stack. 0 distance is center of axial valley. Arrow on lower border shows location of the shot used for the spectrum in Figure 18a. b. Higher migration velocity version of Line 4B after running stack. 0 distance at center of axial valley. Arrow on bottom border shows location of shot used for the spectrum in Figure 18c.

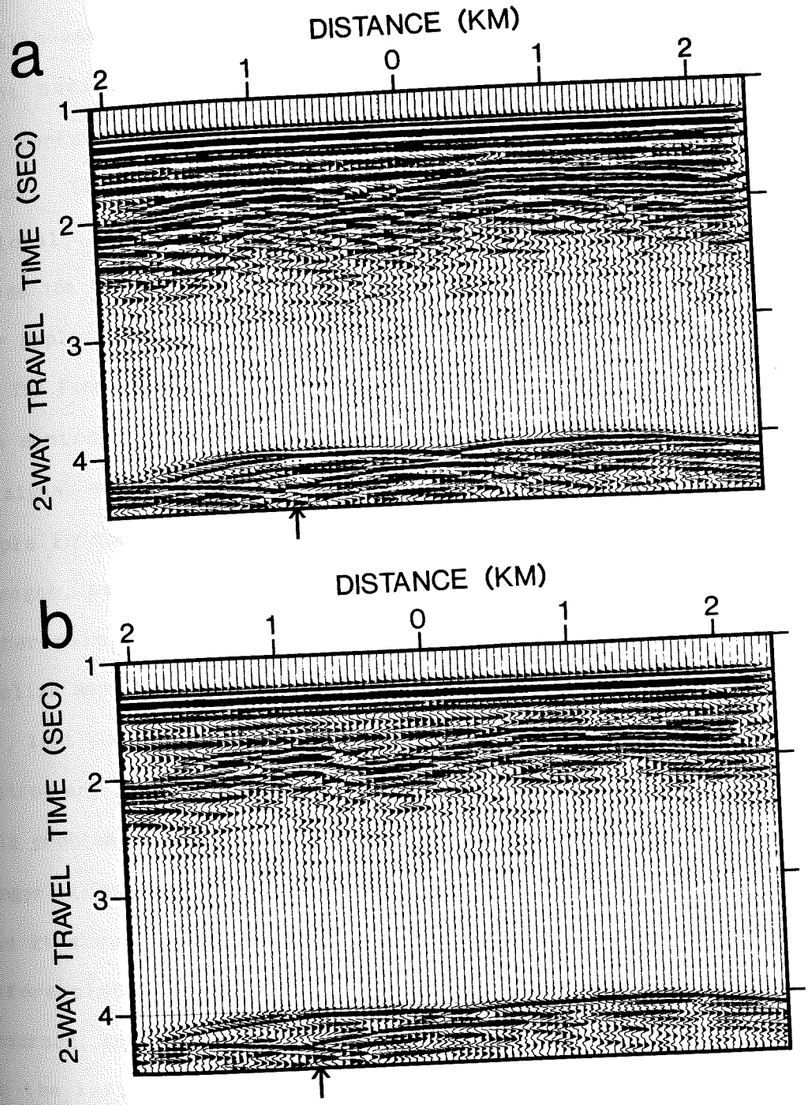

Although the need for an additional stage of band pass filtering is not obvious from an examination of Figures 17a and 17b, experimentation showed it to improve the results of automatic gain control. The same band pass filter was used as had been applied previously. Representative line spectra of the data can be seen in Figures 18a - 18d. Figures 19a and 19b show the data for Line 4B after application of the filter.

The final stage in processing the data was to apply automatic gain control, or AGC. In AGC, each sample is amplified depending on the signal strength within a window of fixed length centered about the sample in question. The gain is inversely related to the signal strength, so that portions of a trace with weak signals will get higher gain than portions with strong signals. The net effect is to equalize amplitudes along the trace. Care must be taken when applying AGC, lest too short of a window be used. Extremely short windows will destroy any local variations in signal strength. Towards avoiding this problem, a long window of 1200 milliseconds was used on the data. Longer windows preserve local variations in amplitude. Figures 20a and 21 show the final result for Line 4B, after application of AGC. Before plotting these final results, the order of the shots was reversed, so that the profiles appear with east on the right, and west on the left. This makes the profiles consistent with the final results for the other lines, and with the standard practice of displaying east-west profiles as if they are being viewed from the south.

Although the need for an additional stage of band pass filtering is not obvious from an examination of Figures 17a and 17b, experimentation showed it to improve the results of automatic gain control. The same band pass filter was used as had been applied previously. Representative line spectra of the data can be seen in Figures 18a - 18d. Figures 19a and 19b show the data for Line 4B after application of the filter.

The final stage in processing the data was to apply automatic gain control, or AGC. In AGC, each sample is amplified depending on the signal strength within a window of fixed length centered about the sample in question. The gain is inversely related to the signal strength, so that portions of a trace with weak signals will get higher gain than portions with strong signals. The net effect is to equalize amplitudes along the trace. Care must be taken when applying AGC, lest too short of a window be used. Extremely short windows will destroy any local variations in signal strength. Towards avoiding this problem, a long window of 1200 milliseconds was used on the data. Longer windows preserve local variations in amplitude. Figures 20a and 21 show the final result for Line 4B, after application of AGC. Before plotting these final results, the order of the shots was reversed, so that the profiles appear with east on the right, and west on the left. This makes the profiles consistent with the final results for the other lines, and with the standard practice of displaying east-west profiles as if they are being viewed from the south.

Figure 18. a. Representative line spectrum of lower migration velocity version of Line 4B (see Figure 17a for location of shot). b. Post-filtering line spectrum of the shot used in panel a (see Figure 19a for location). c. Representative line spectrum of higher migration velocity version of Line 4B (see Figure 17b for location). d. Post-filtering line spectrum of the shot used in c (see Figure 19b for location).

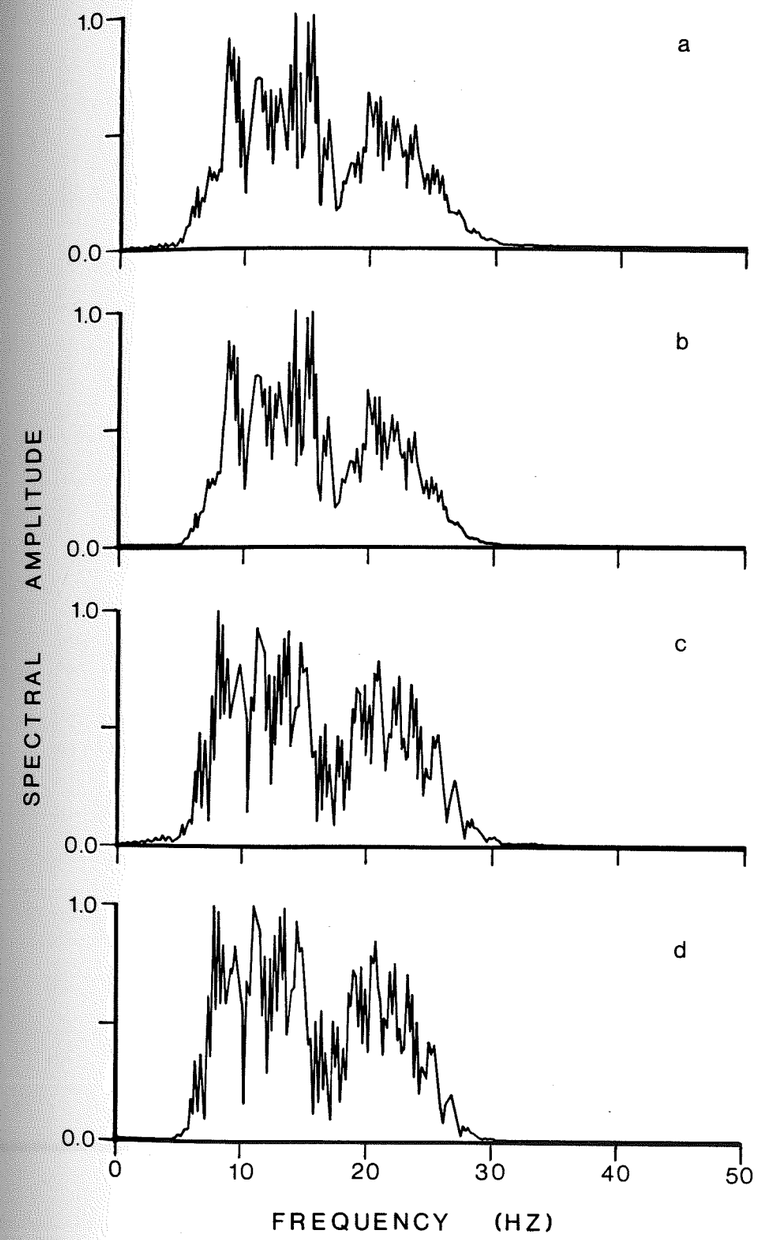

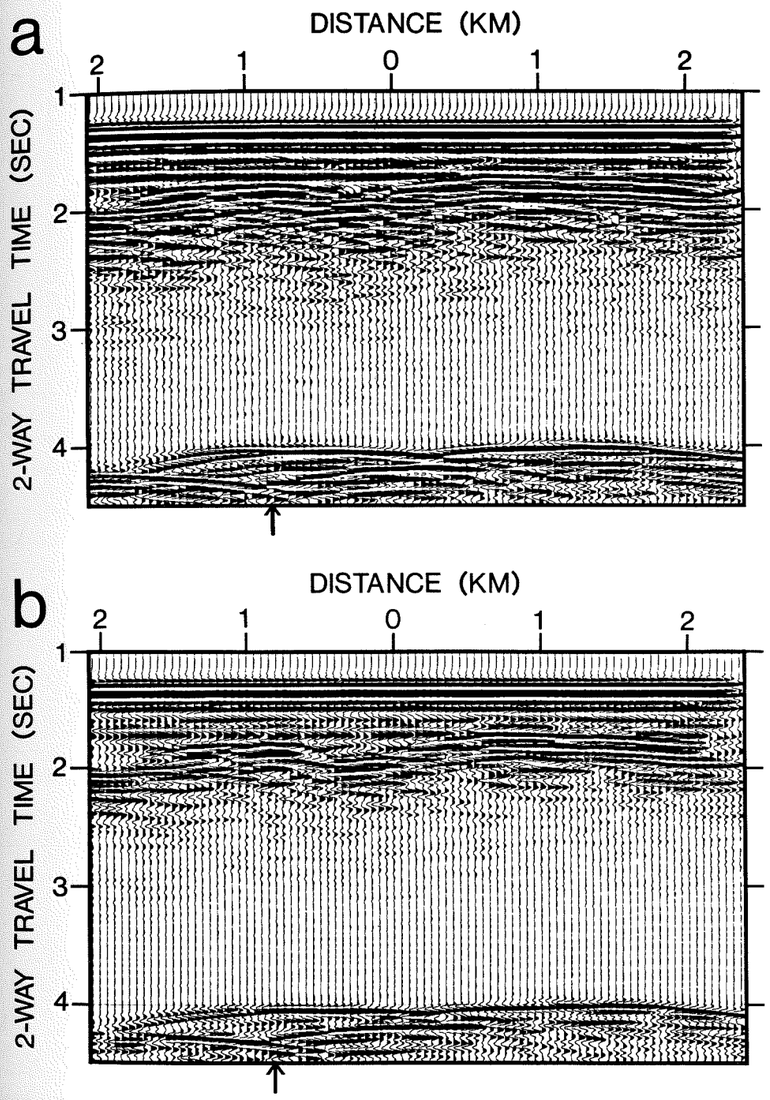

Figure 19. a. Results of filtering the data in Figure 17a (low velocity version of Line 4B). Arrow at bottom shows the shot used for the spectrum in Figure 18b. b. Results of filtering the data in Figure 17b (high velocity version of Line 4B). Arrow indicates the shot used for the spectrum in Figure 18d. In both panels, 0 distance is at the midlle of the axial vallley.

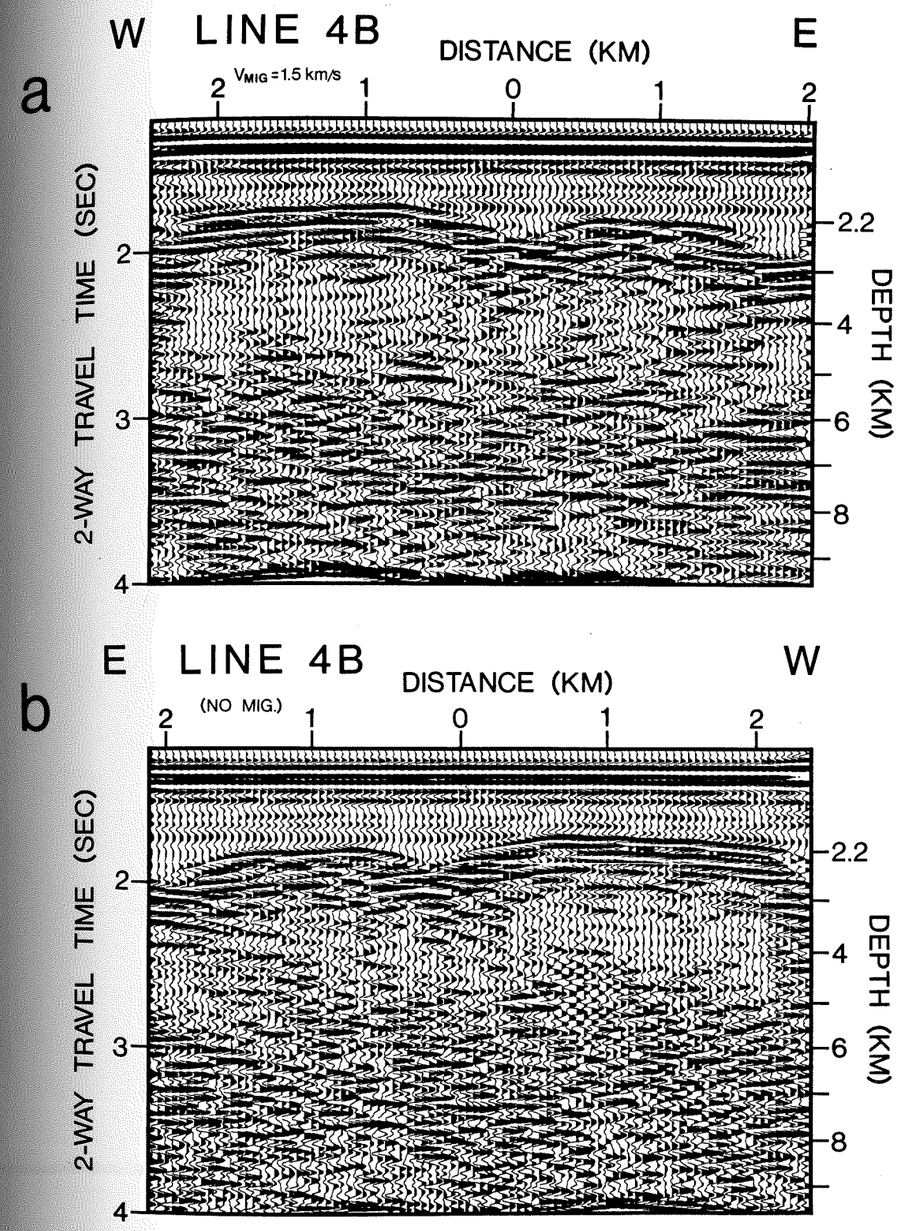

Figure 20. a. Results of applying AGC to the data in Figure 19a (low velocity version of Line 4B). The profile in this panel has been reversed so that east is now on the right of the figure. b. The data in this figure has been processed identically to the data in panel a and to the data in Figure 21, with the exception that it has not been migrated. (This profile has not been reversed, so that east is on the left of the figure.) The presence of the layered features in the lower crust shows that these features are not artifacts on the migrated profiles. In both panels, 0 distance is at the center of the axial valley.

Figure 21. Final processed version of Line 4B. The higher mid-crustal migration velocity has been used. This profile has been reversed so that E is on the right; 0 distance is at the center of the axial valley.

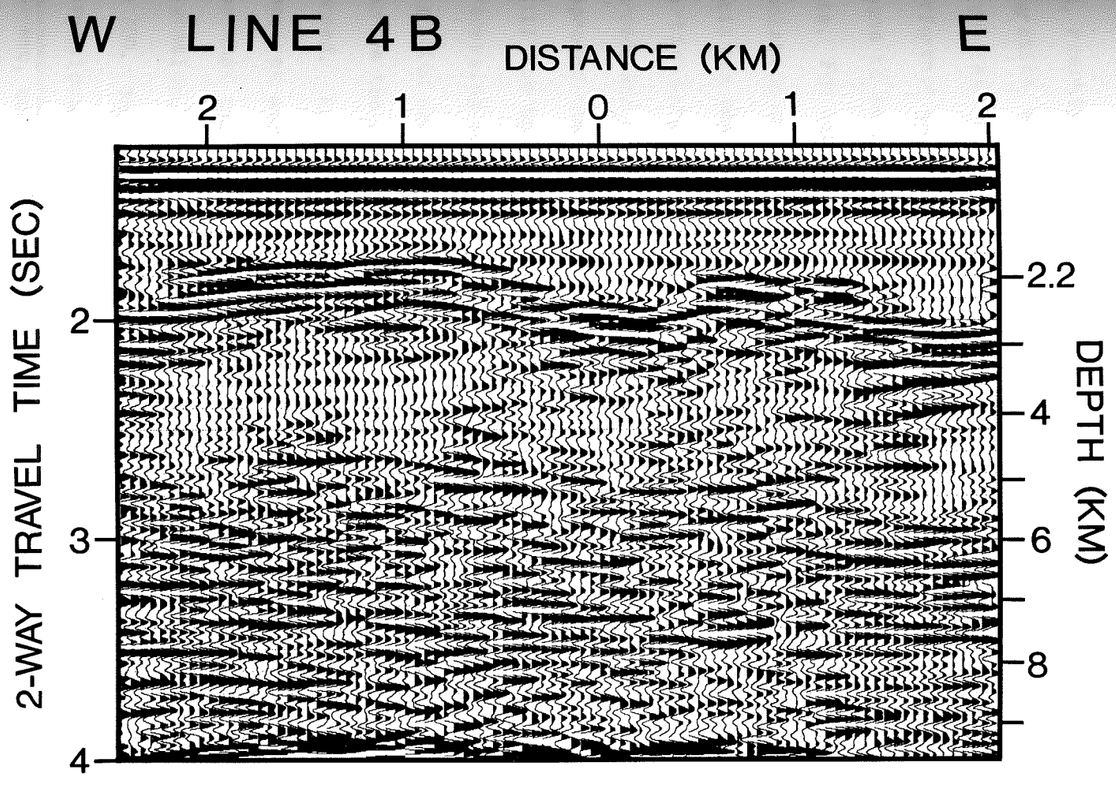

Final results for Lines 1A, 2A, 1B, 3B, and 8A are in Figures 22-26, respectively. For all of these profiles, the higher, mid-crustal migration velocity was used. The processing for Lines 1A and 2A differed from that of the other lines in three ways. The first difference was that the data were not deconvolved. Deconvolution was found to be unreliable owing to the poor signal to noise ratio of the data. For Lines 1A and 2A, only one airgun was used, and mechanical isolation of the streamer was poorer, so that a lower signal to noise ratio was unavoidable. Some of the problem was alleviated by zeroing particularly noisy traces. For Line 1A, 30% of the traces were zeroed, and for Line 2A, 45% of the traces were zeroed. Although this improved the appearance of the profiles, the remaining traces were still too noisy for deconvolution. The second difference in the processing of Lines 1A and 2A was that the group stacking prior to migration was done by nine's instead of by eight's. This was done to improve the results of the stacking, since the noisier traces had been zeroed. At this point, peak amplitudes from trace to trace were compared and trace amplitudes were normalized. The third difference was that the data for Lines 1A and 2A were subsampled prior to migration. The sampling rate was reduced from 800 samples per second to 200. This was done to reduce the computation time during the two dimensional transform. Subsampling was done after the data had been stacked, and after a band pass filter was applied. The filter was a cascaded 10 pole Butterworth with a high frequency setting of 40 Hz.

Figure 22. Final processed version of Line 1A. Processing is the same as that applied to Line 4B, except that Line 1A was not deconvolved. 0 distance is the center of the axial valley.

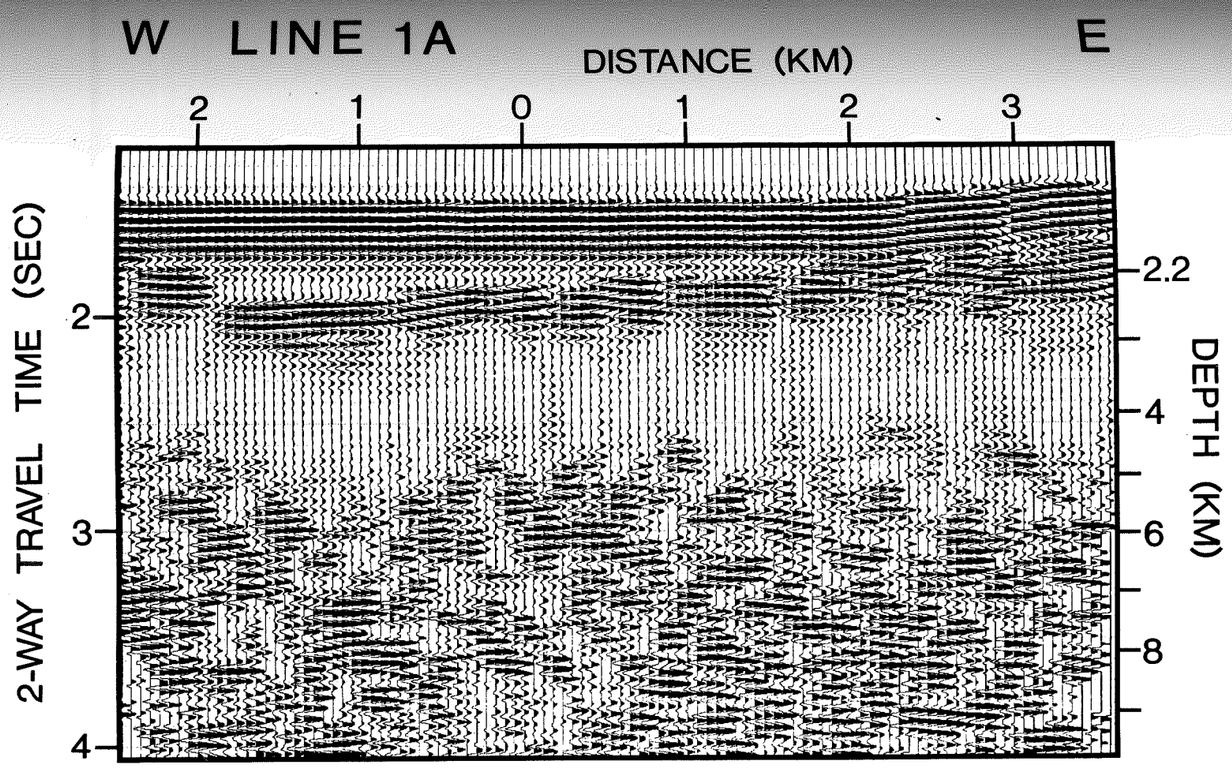

Figure 22. Final processed version of Line 1A. Processing is the same as that applied to Line 4B, except that Line 1A was not deconvolved. 0 distance is the center of the axial valley.

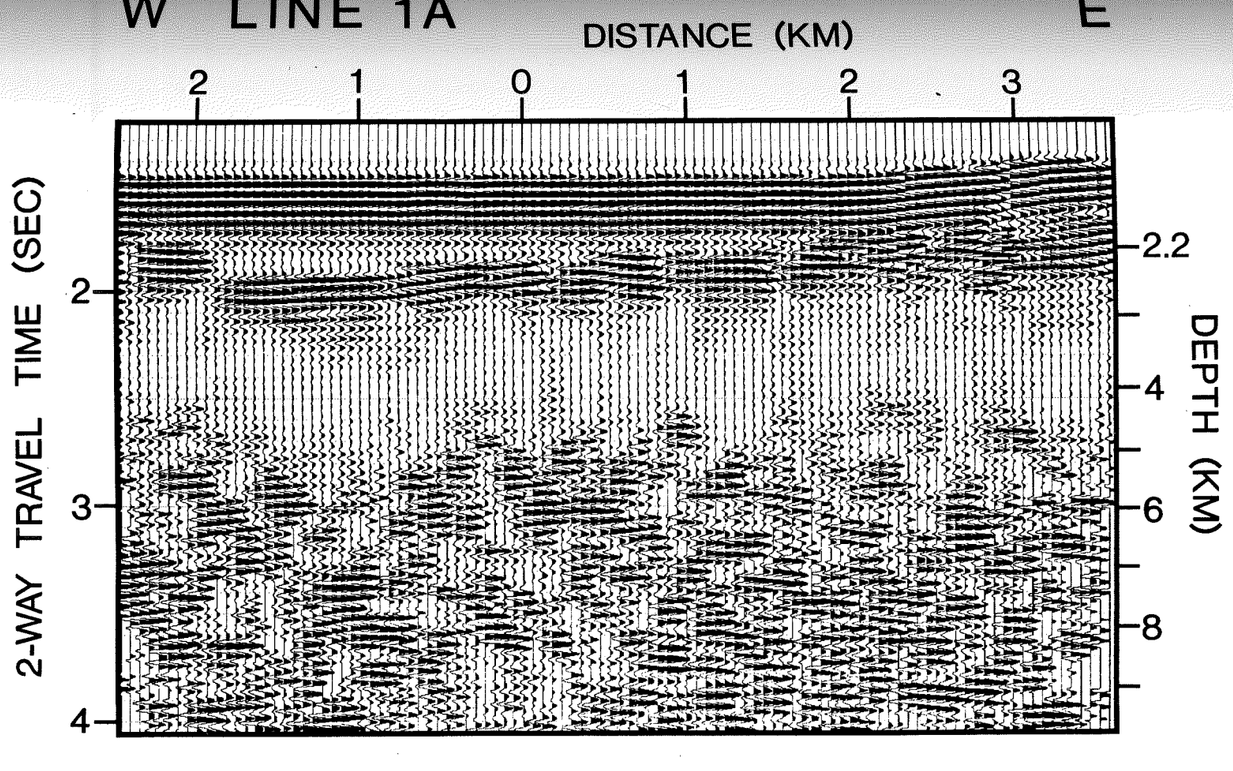

Figure 23. Final processed version of Line 2A. Processing is the same as that applied to Line 4B, except that Line 2A was not deconvolved. 0 distance is the center of the axial valley.

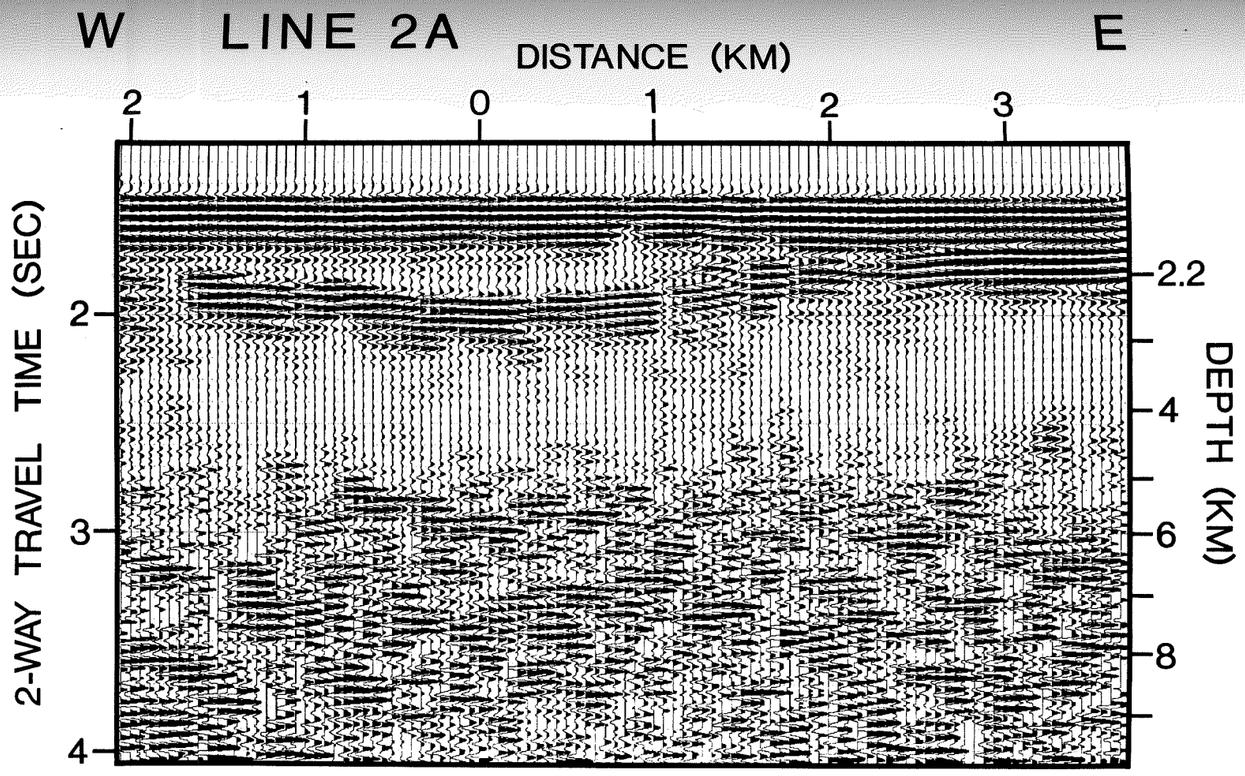

Figure 24. Final processed version of Line 1B. Processing was the same as Line 4b, except that a spiking deconvolution filter was used. 0 distance denotes the middle of the axial valley.

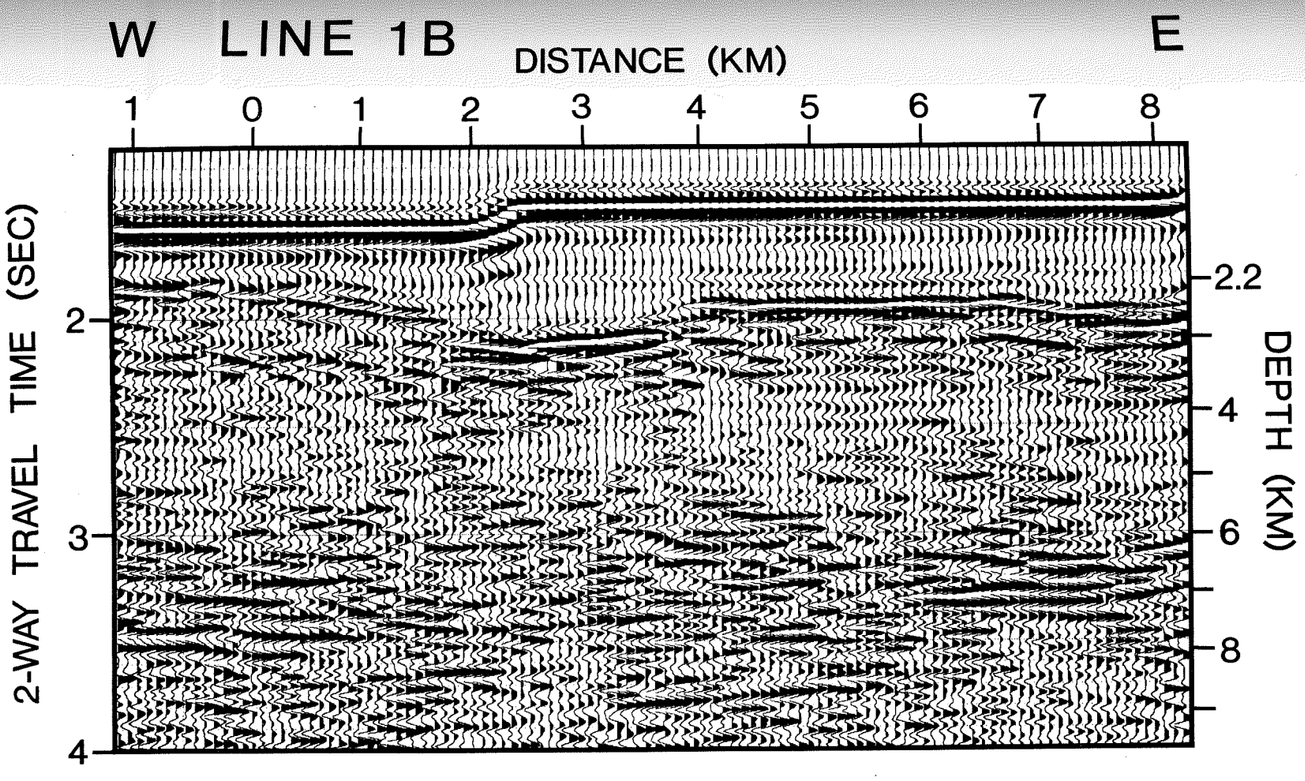

Figure 25. Final processed version of Line 3B. Processing was the same as Line 4B. 0 distance is the center of the axial valley. The sea floor appears at a two-way travel time of 1.7 seconds on the extreme right and left of the profile, and also at 0 distance; in between these points, the sea floor shoals and merges with the direct water wave.

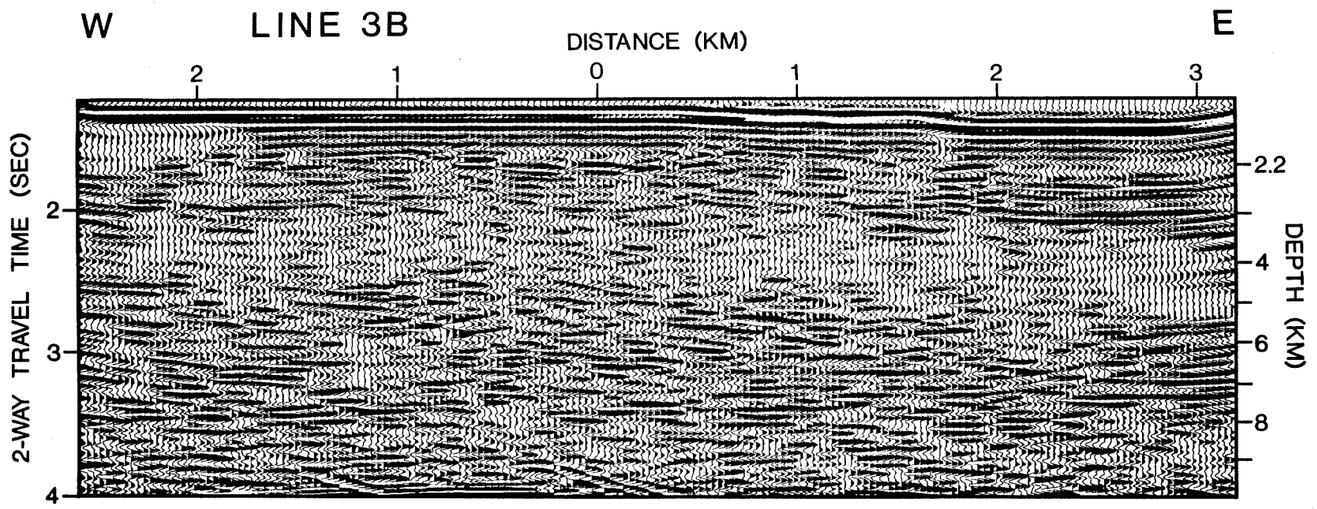

Figure 26. Final processed version of Line 8A. Processing was the same as Line 4B. 0 distance is the center of the axial valley.

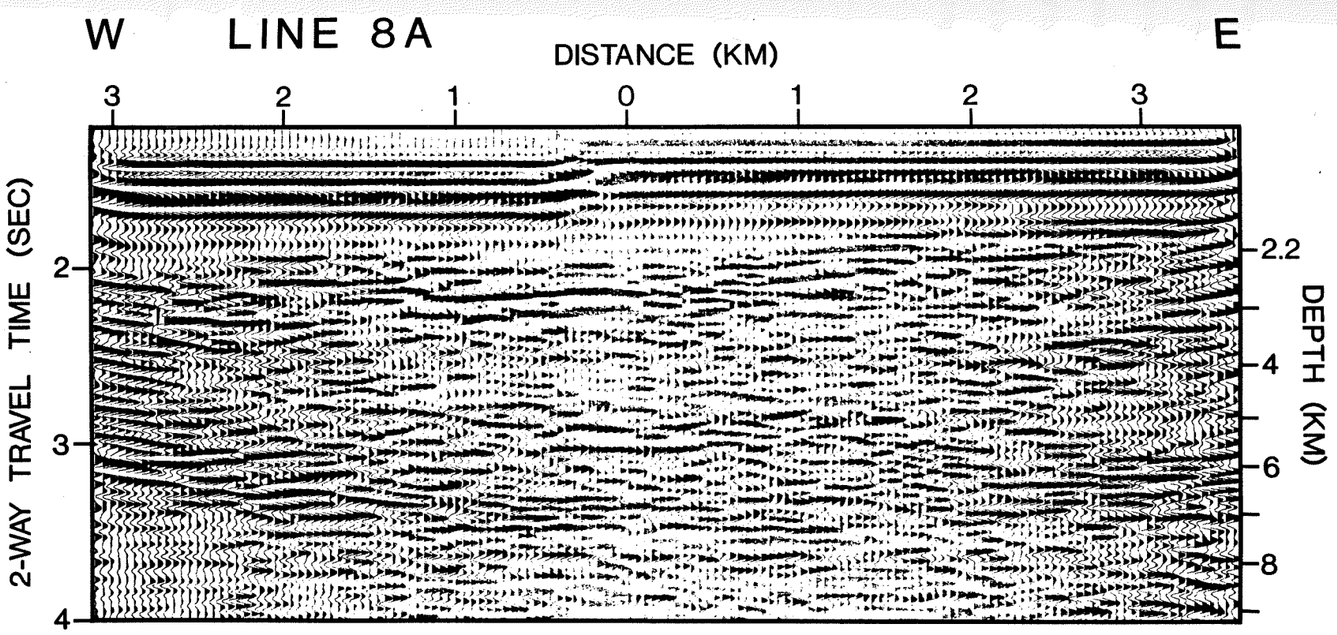

Since the final Nyquist frequency was 100 Hz, this filter prevented aliasing during subsampling.

Tables 2 - 5 describe the processing techniques applied to the six lines. Table 2 is a general summary of the steps applied to each line. Filtering parameters are contained in Table 3. In Table 4, deconvolution parameters are collated, and in Table 5, miscellaneous processing parameters are collected.

Table 2. Summary of Data Processing.

	Line Number					
	1A	2A	1B	3B	4B[1]	8A
Preliminary Manipulations[2]	x	x	x	x	x	x
Band Pass Filtering[3]			x	x	x	x
Deconvolution[4]			x	x	x	x
Group Stack[5]	x	x	x	x	x	x
Band Pass Filtering[3]	x	x	x	x	x	x
Padding (and Subsampling)[6]	x	x	x	x	x	x
Migration[7]	x	x	x	x	x	x
Running Stack[8]	x	x	x	x	x	x
Band Pass Filtering[3]	x	x	x	x	x	x
Automatic Gain Control[9]	x	x	x	x	x	x

NOTES:
1. The order of the shots in Line 4B was reversed after processing so that east was on the right side of the plot. This was done so that Line 4B would be consistent with the other lines.
2. For Lines 1A and 2A: zeroing of noisy traces. For Lines 1B, 3B, 4B, and 8A: registration or justifying of traces with erroneous recording window onsets.
3. For each line, the same filter was used throughout. See Table 3 for a summary of filter parameters.
4. See Table 4 for a summary of deconvolution parameters.
5. Lines 1A and 2A were (group) stacked by 9's. After this, the amplitudes of the various traces were normalized. The other lines were stacked by 8's.
6. For a summary of final sample rates, final number of samples per trace, and number of traces input to migration, see Table 5.
7. Migration for the final plots of all lines was with a velocity of 2.4 kilometers per second.
8. A running stack of three shots was used on all lines.
9. An automatic gain control window of 1200 milliseconds was used on all lines.

Table 3. Band Pass Filters.

LINE	POLES (#)	LOW CUT (Hz)	HIGH CUT (Hz)
1A	10	16.5	40.0
2A	10	16.5	40.0
1B	6	6.0	30.0
3B	6	6.0	30.0
4B	6	6.0	28.0
8A	6	6.0	25.0

NOTES: All filters were Butterworths, and all were cascaded. A higher number of poles was used on Lines 1A and 2A so that the steeper filter response would allow elimination of low frequency cable strum and ship heave noise, without affecting the spectrum of the seismic pulse.

Table 4. Deconvolution Parameters.

LINE[1]	DESIRED OUTPUT	DESIGN WINDOW LENGTH[2] (sec)	OPERATOR LENGTH (sec)	PRE-WHITENING (percent)	OUTPUT LAG (samples)
1B	([3])	2.0	0.3	1.0	20
3B	([4])	2.0	0.3	0.1	20
4B	([4])	2.0	0.2	1.0	20
8A	([4])	2.0	0.3	0.1	20

NOTES:
1. The data for Lines 1A and 2A was not deconvolved.
2. For each line, the start of the design window was chosen so as to coincide with the onset of the direct water wave.
3. Line 1B was deconvolved with a spiking filter.
4. Lines 3B, 4B, and 8A were deconvolved with wave shaping filters, with the desired output pulse shape shown in Figure 13.

Table 5. Miscellaneous Data Processing Parameters.

LINE	SUBSAMPLING	FINAL SAMPLING RATE (sam/sec)	GROUP STACKING FACTOR	FINAL SHOT SPACING (meters)	# OF SAMPLES PER TRACE FOR MIGRATION	# OF TRACES FOR MIGRATION
1A	Yes	200	9	60	1024	256
2A	Yes	200	9	56	1024	256
1B	No	100	8	82	512	256
3B	No	100	8	31	512	512
4B	No	100	8	49	512	256
8A	No	100	8	46	512	256

Chapter 4

Results

This chapter is a preliminary analysis of the processed data. The profiles are compared and discussed in terms of reliability of the information they contain. Interpretation and scientific discussion of the data are contained in the next chapter. In the first part of this chapter, the reliability of the data is dealt with; are the reflectors real? The second part of this chapter is a review of how depth sections, reflection geometries, and the timing of multiples were calculated.

Preliminary Discussion

The final processed profiles in Figures 21 - 26 are all very similar in that the upper crust is relatively transparent, while the lower crust is well layered. Is the transparency of the upper crust real, or is it an artifact of the AGC? A gain window centered on a sample from the upper crust would see the high amplitude reflections from the ocean floor, and these reflections would dominate the window, leading to a low gain factor. Windows centered on samples from the lower crust would not be dominated by such high amplitude reflections, and would have higher gain factors. This sort of an effect could make the upper crust appear transparent. To resolve this issue, a test was devised and performed on each line.

The basis of the test was to examine the reflection amplitudes of the migrated, ungained data, and see if any jump in amplitudes existed at the point where the layering in the lower crust appeared. One way

to do this is to apply a regular, smoothly varying gain function to the data and examine the results. Visual inspection of individual data traces showed a roughly exponential decay in reflection amplitudes, and for this reason it was decided to use an exponential curve as the smooth gain function. The time constant of the exponential curve was determined by the following sequence of five steps. First a given data trace was windowed so as to remove the direct water wave and the multiples. Next the absolute values of the reflection amplitudes were summed in a 10 sample long window which was moved through the data. In the third step, the summed window values were smoothed by three's. Then the smoothed values were normalized to the first value in the sequence, and natural logarithms were taken. Finally, the last step was to perform a linear regression on the resulting values. The linear regression provided the time constant for the desired gain function, and also gave information as to the correctness of the choice of an exponential as the function. On average, regression coefficients for the fit of an exponential to the decay of reflection amplitudes were better than (-)0.95.

The procedure described above was used on four successive traces from each profile, and the resulting time constants were used to apply gain to the traces. The results are shown in Figures 27 and 28; in most all cases, at two-way travel times of approximately 1 second, there exists a jump in reflection amplitudes. This then shows that the relative transparency of the upper crust in the processed profiles

Figure 27. Results of the gain test for Lines 1A, 2A, and 1B. On most all of the traces there is a jump in amplitudes at roughly 1 second relative to the background exponential increase.

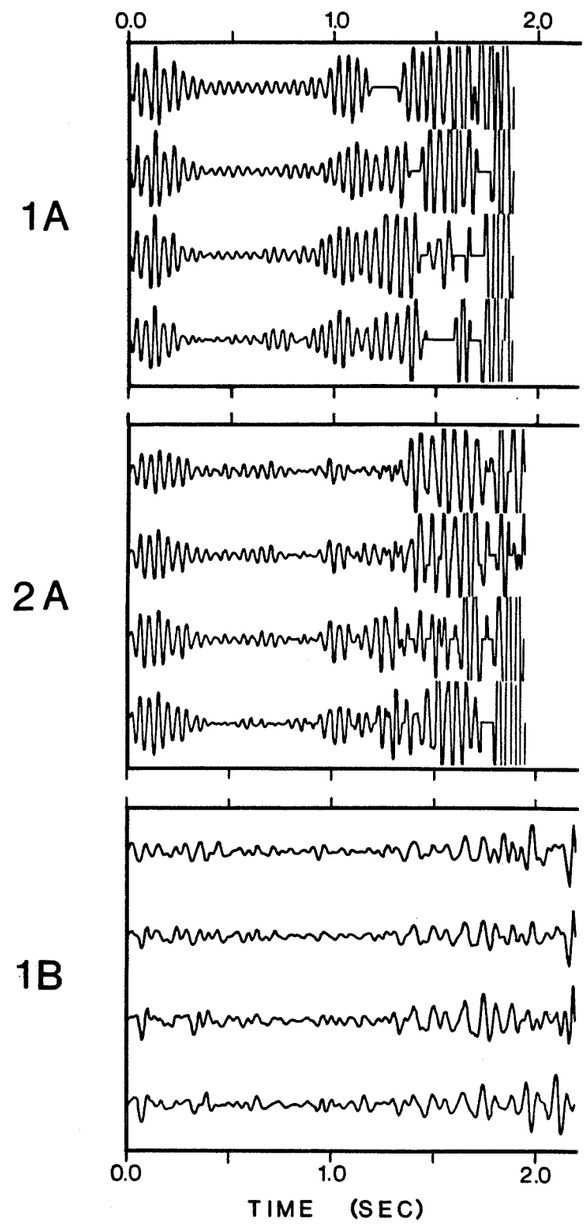

Figure 28. Results of the gain test for Lines 3B, 4B, and 8A. On many of the traces there is a jump in amplitudes at roughly 1 second, relative to the background exponential increase.

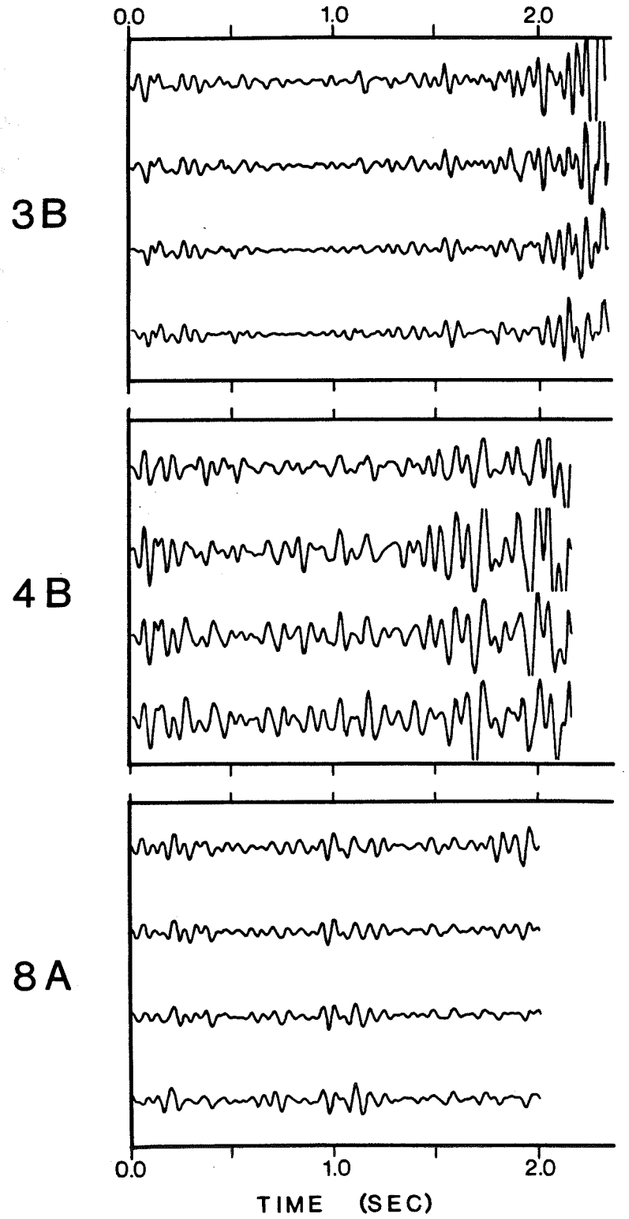

is real, and not an artifact of the AGC. It should be noted however, that the AGC has likely had the effect of enhancing this appearance.

Before concluding that the reflectors in the processed profiles are real, there are other alternative interpretations to be considered. First among them is the possibility that the apparent reflectors are converted phases. For instance, shears waves generated by conversion at the sea floor could be reflected from some shallow crustal interface and be returned to the hydrophones at the observed time of approximately one second. This is highly unlikely for two reasons. The first is that the shallow crustal interface reflecting the shear waves would also reflect any compressional waves, and there are no strong reflections from that part of the crust. Secondly, there is a problem with amplitudes. For the shear waves to be returned to the hydrophone, they would have to be reconverted to compressional waves at the sea floor on the upward limb of the ray path. Since converted phases are considerably weaker than incident phases, and the energy reaching the hydrophone at one second would have been converted twice, we would expect very weak reflections. However, the reflectors seen at one second sub-bottom time are relatively strong, and hence, it can be concluded that these are not converted phases.

Another alternative explanation of the reflectors in the processed profiles is that they are higher order multiples. There are four reasons that this alternative can be discounted. The first reason is that all six profiles have very much the same structure.

The timing of multiples depends on the reflection geometry; how far behind the source the streamer is, and for the case of the Deep Tow, the vertical offset between the source and streamer. Variations in the geometry would cause the multiple to be advanced or delayed. For each profile, the geometry was different, yet the timing of the possible multiple is the same (the reflection geometry is discussed in more detail later in this chapter). The second reason that multiples can be discounted has to do with the shot schedule of the various profiles. Lines 1A and 8A were taken at very nearly the same location in Area A. The reflection geometries and the bathymetry for the two profiles are similar, but the shot schedule for Line 1A was 10 seconds, while that for Line 8A was 11 seconds. Since the multiple on a given shot would have to be from a previous shot, the longer shot schedule on Line 8A should have the effect of advancing the suspected multiple in the recording window. However, no such difference between the two profiles is seen. The third reason for discounting higher order multiples comes from an analysis of the expected arrival times of these multiples. Based on the reflection geometry, and assuming a flat sea floor, the travel time of several successive higher order multiples was calculated. The lowest order multiple that was found to occur at the appropriate time in the recording window was a 15th order multiple (one that has been reflected 15 times from either the sea floor or the sea surface). Multiples of this high an order can be neglected because lower order multiples occurring at quiet times in the recording window were found to be of negligible amplitude.

Finally, the fourth reason for discounting multiples has to do with the shape that a multiple takes. The primary multiple shows a vertically exaggerated sea floor; that is, the sea floor relief is exaggerated by a factor of two. Successively higher order multiples will show successively greater exaggeration of sea floor relief. High order multiples would be be extremely exaggerated, and not at all like the relatively smooth horizons of reflectors seen in the lower crust of the processed profiles.

The last alternative explanation for the apparent layering in the lower crust of the processed profiles is that the apparent reflectors are processing artifacts. The possibility that the apparent reflectors are artifacts of the AGC has already been discussed and discounted. There are two other main steps in the processing where such artifacts could have arisen; deconvolution and migration. Deconvolution as a source of artifacts can be discounted because Lines 1A and 2A were not deconvolved, yet they display the same general features as Lines 1B, 3B, 4B, and 8A. Migration can be dismissed since the features enhanced by it are evident without its application. Figure 20b shows the data for Line 4B without migration. The same series of processing steps was applied to the data, up until migration. At this point a running stack by three's and AGC were applied, so as to mimic the the post-migration processing applied to the line as presented earlier. In Figure 20b, the lower crust again displays extensive layering, although not as clearly as for the

migrated data. This shows that the structure seen on the processed profiles is not a migration artifact.

Depth Sections

The final processed profiles in Figures 21 - 26 have been presented with dual vertical axes, one for two-way travel time and one for depth. In this part of the chapter the conversion from time to depth sections is discussed. Preparatory to this is a discussion of the reflection geometries and the calculation of multiple timing. The chapter is concluded with a discussion of the error analysis for the uncertainties in the geometry and depth calculations.

Figure 29 shows the model used to calculate reflection geometries. The model assumes a flat ocean floor and a plane layer ocean with a compressional wave velocity of 1.5 kilometers per second. The three variables are X, the horizontal offset between the source and the streamer, Z, the water depth, and H, the height of the streamer off the sea floor. Calculating these three variables required three measurements, which were the travel time for the direct water wave, the travel time of the sea floor reflection, and the travel time of the first direct multiple. These three time measurements were taken at eight equally spaced locations along each profile, and used to obtain eight sets of calculated X's, Z's, and H's. An average geometry for the profile was then obtained from these eight sets. This information is summarized in Table 6. The calculated reflection geometries and the plane layer ocean model were in turn used to calculate the travel time of higher order multiples.

Figure 29. Diagram showing the model used for calculating reflection geometries. The model assumes a plane layer ocean with a velocity of 1.5 kilometers per second. X is the horizontal offset of the receiver (R) behind the source (S). Z is water depth, and H is the height of the receiver off the sea floor. The quantities measured in order to calculate the three unknowns X, Z, and H, are: D, the direct water wave travel time (shown with a heavy dashed line); P, the primary sea floor reflection travel time (shown with a heavy solid line); and M the first order multiple travel time (shown with an intermediate weight dashed line).

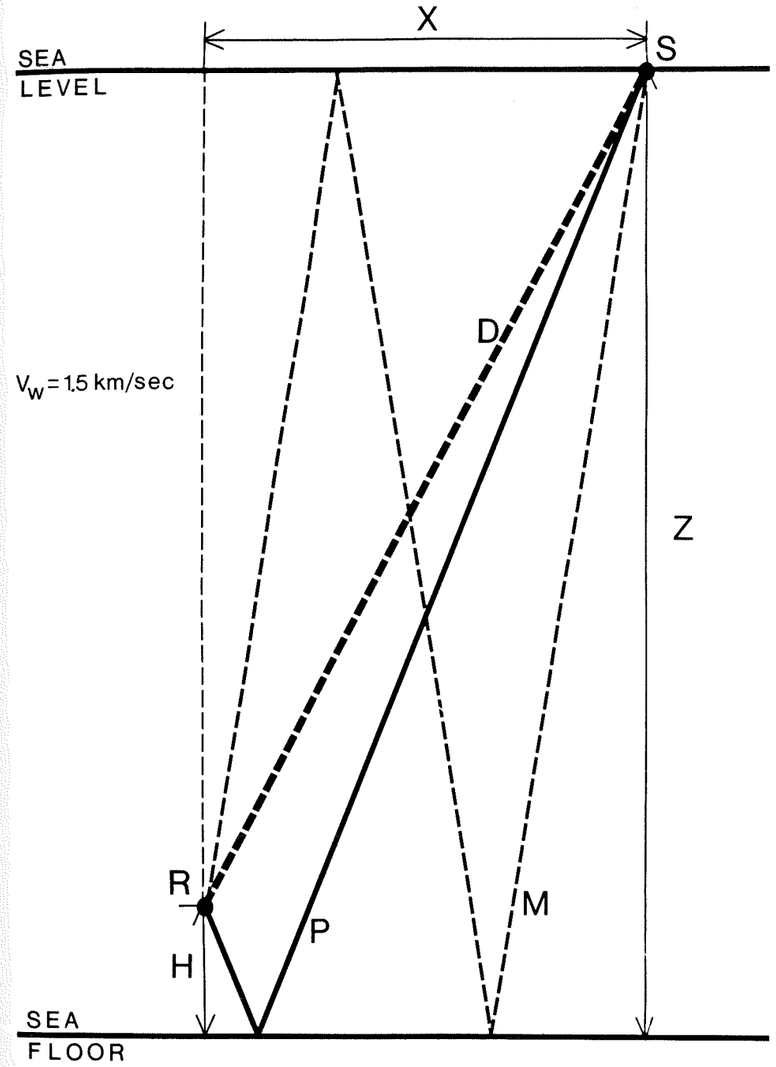

Table 6. Reflection Geometry.

LINE	HORIZONTAL OFFSET (km)	WATER DEPTH (km)	STREAMER HEIGHT (km)
1A	1.0	2.2	0.3
2A	1.1	2.2	0.3
1B	1.2	2.2	0.4
3B	0.7	2.2	0.3
4B	1.1	2.2	0.4
8A	1.0	2.2	0.5

The approach used to convert the profiles to depth sections was to calculate the depth to a given travel time and then generate a non-linear depth axis to be superimposed on the linear two-way travel time axis. This was done with the same plane layer ocean model of velocity 1.5 kilometers per second, and with the crustal velocity model shown in Figure 30 [H. Jung, personal communication, 1988]. In calculating the travel time to a given depth, the hybrid reflection geometry has to be taken into account, in particular the horizontal offset. To perform the calculations, a crude computer ray tracing program was developed with inputs of the reflection geometry and an approximation to the velocity model consisting of 0.1 kilometer thick plane layers of crust with constant velocities. Calculating the travel time for a depth corresponding to the bottom of a given layer was a matter of finding the ray path which connected the source and streamer via a reflection off the bottom of the layer. Travel times and depths for each layer were collated and then used to generate the non-linear depth axes for the profiles. The results can be seen on the final processed profiles in Figures 21 - 26.

The depth axes described above should be taken as approximate ones, as there are several sources of errors in the calculations. First of all, the reflection geometry could be in error for various reasons. The measured travel times could be incorrect; the assumed water column velocity of 1.5 kilometers per second could be in error; or deviations from the plane layer ocean model could be important. To estimate the effect of timing and velocity errors, a timing

Figure 30. The upper crustal velocity model used for calculating depth axes for the final processed profiles. A constant lower crustal velocity of 7.22 kilometers per second was used. [Source: H. Jung, personal communication, 1988.]

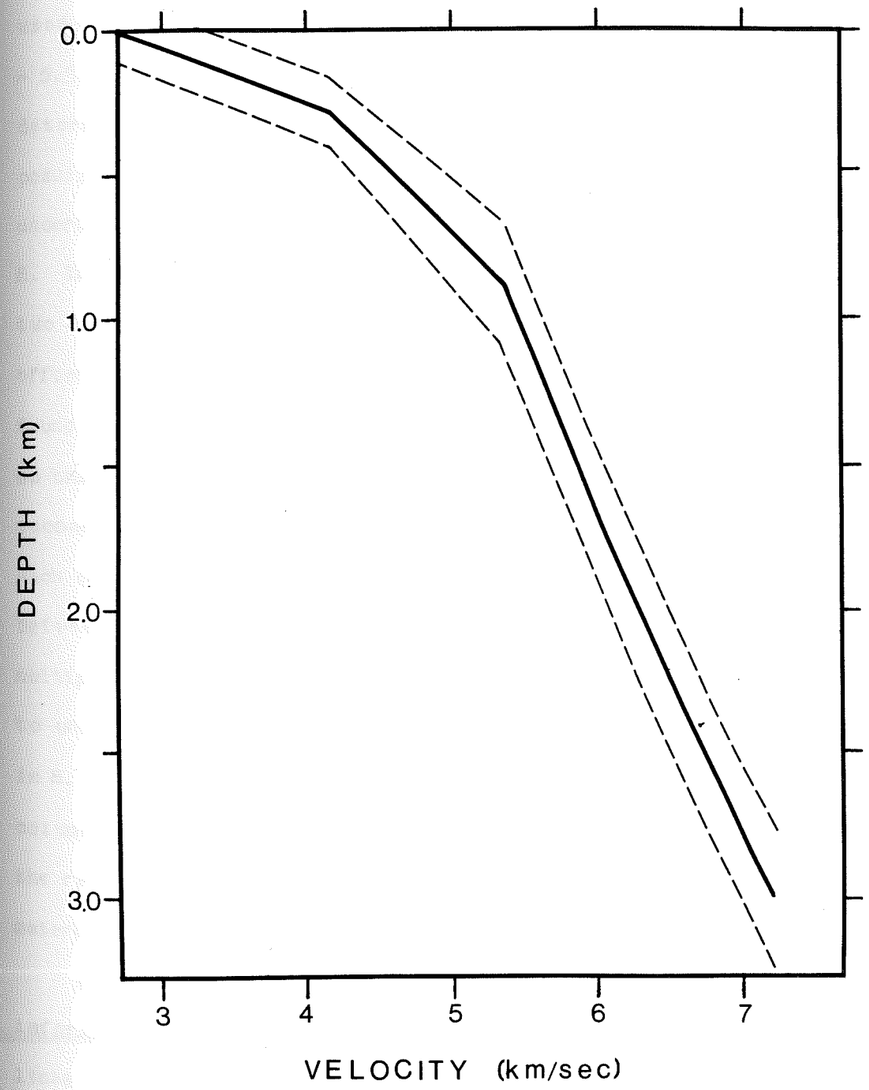

uncertainty of ±0.02 second and a velocity uncertainty of ±1% were used in a test case with X = 1.0 kilometer, Z = 2.2 kilometers, and H = 0.3 kilometers. For this test model, the exact travel times were determined and compared to travel times calculated by permuting the possible errors. In the worst possible case, the timing and velocity uncertainties were found to create an error of ±70 meters in X, Z, and H. To test the effect of deviations from the plane layer ocean model, two cases were considered, both of which involved a 100 meter step offset in ocean floor topography, which is the size of the offsets found on the real profiles. The first case was with the step arranged so that the water was 100 meters deeper under the source, and the second case had the water 100 meters shallower under the source. In each case the lateral position of the step was set so that it was between the points where the sea floor reflection and the direct multiple interacted with the sea floor. The worst configuration led to uncertainties of ±170 meters in X, ±70 meters in Z, and ±10 meters in H. In the worst case then, the additive effects of timing, water column velocity, and model deviations would lead to uncertainties in the reflection geometry of ±240 meters in X, ±140 meters in Z, and ±80 meters in H.

The other main source of error in generating the depth section information is from uncertainties in the velocity model. The dashed lines in Figure 30 show upper and lower bounds for the velocity at a given depth. With the temporary assumption that the reflection geometry was correct, the effects of velocity uncertainties on the

depths for given travel times were estimated by using the ray tracing program with inputs of the upper and lower bounds for the velocity model. It was determined that velocity model uncertainties could lead to depth errors of at most ±300 meters. Next the effects of errors in the reflection geometry were estimated, assuming that the velocity model was correct. The geometry errors were permuted and then run through the ray tracing program. The result was that geometry errors could lead to depth errors of at most ±300 meters. Finally, the combined effects of geometry and velocity errors were estimated, in the same manner, by permutation with the ray tracing program. It was found that the combined effects of velocity and geometry uncertainties could lead to depth errors of at most ±500 meters. The depth errors are least at shallow depths below the ocean floor, increasing rapidly with depth until the roughly constant error of ±500 meters is reached after ~1/2 second of two-way travel time. A summary of the error analysis can be found in Table 7.

Table 7. Summary of Error Analysis.

I. Reflection Geometry

Source of Uncertainty	Resulting Error X (m)	Z (m)	H (m)
A. Water Column Velocity and Time Measurements	±70	±70	±70
B. Deviation from Plane Layer Ocean Model	±170	±70	±10
C. Additive Effects of I A & B	±240	±140	±80

II. Depth Sections

Source of Uncertainty	Resulting Depth Error (m)
A. Seismic Velocity Model	±300
B. Reflection Geometry	±300
C. Combined Effects of II A & B	±500

Chapter 5

Discussion

This chapter begins with the discussion and interpretation of the features seen in the processed profiles. The profiles will then be related to current models of crustal generation at ridge crests in order to determine those models which the profiles support.

Processed Profiles

Determining the presence or absence of magma chambers at ridge crests is one of the main objectives of the research in this thesis. Of the six processed profiles, only Line 8A (Figure 26) shows a reflector that could be interpreted as a magma chamber. There is a strong reflector centered beneath the ridge axis at a two way travel time of roughly 3 seconds. This corresponds to a sub-bottom travel time of 1 second, or a sub-bottom depth of approximately 2.5 - 3.0 kilometers. The width of the reflector is on the order of 1 kilometer. The depth and width of this reflector correlate well with a similar feature seen on a multichannel profile collected by Morton et al. [1987] farther south on this segment of the JDF (Figure 31; see Figure 3 for the track line of the multichannel profile). The reflector on 8A also occurs at roughly the same depth as features seen with seismic reflection techniques on the East Pacific Rise at several locations [Herron et al., 1978; Herron et al., 1980; Hale et al., 1982; Detrick et al., 1987], and on the Valu Fa Ridge near Fiji [Morton and Sleep, 1985].

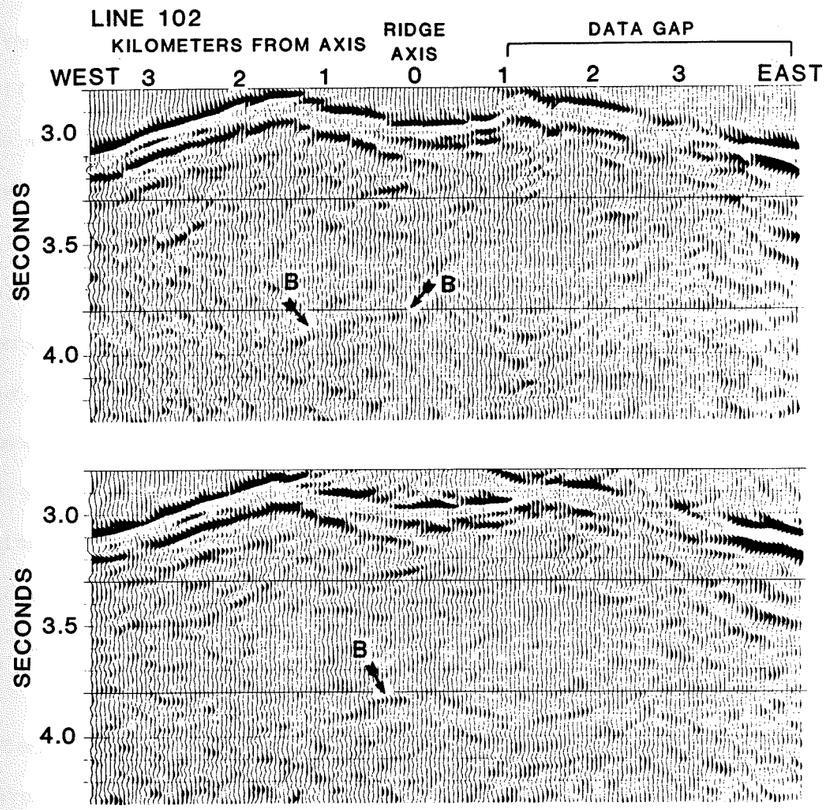

Figure 31. Multichannel reflection data from the southern Juan de Fuca (From Morton et al. [1987]). See Figure 3 for the track line. The upper panel has been migrated at the water column velocity; The lower panel at a higher mid-crustal velocity of 2.3 kilometers per second. The feature labeled with a B in both panels is the feature of interest.

Line 2A of this thesis crosses the axis of the JDF at nearly the same point as the multichannel profile of Morton et al. [1987], but no similar feature is seen. This discrepancy is not entirely unexpected given the poor signal to noise ratio of the data for Line 2A, and the difficulties that the noise made for during processing. Similarly, the absence of such a feature on Line 1A is also a likely result of high noise levels.

Seismic velocities in a magma chamber would be lower than the velocities in the surrounding rock [Murase and McBirney, 1973]. Therefore, there should be a polarity reversal for reflections from the roof of a magma chamber. Morton et al. [1987] were unable to demonstrate a polarity reversal for their reflector; however, they interpret the reflector as possibly being from a magma chamber. The noise levels in Line 8A, although much improved over those in Lines 1A and 2A, still proved to be too high to allow an accurate determination of the phase of the reflector.

Since the polarity of the reflector in Line 8A could not be determined, the possibility exists that it might have been reversed, which would have indicated that the reflector is a magma chamber. However, the reflector on Line 8A is not interpreted as being from a magma chamber on the basis of seismic refraction data from the area. The refraction line R_1 in Figure 3 was shot in September of 1981, during cruise TT-161 of the R/V Thomas G. Thompson [Brian Lewis, unpublished data]. Figure 32 shows reduced travel time data for ocean bottom seismometers (OBS's) that were situated near the ridge crest

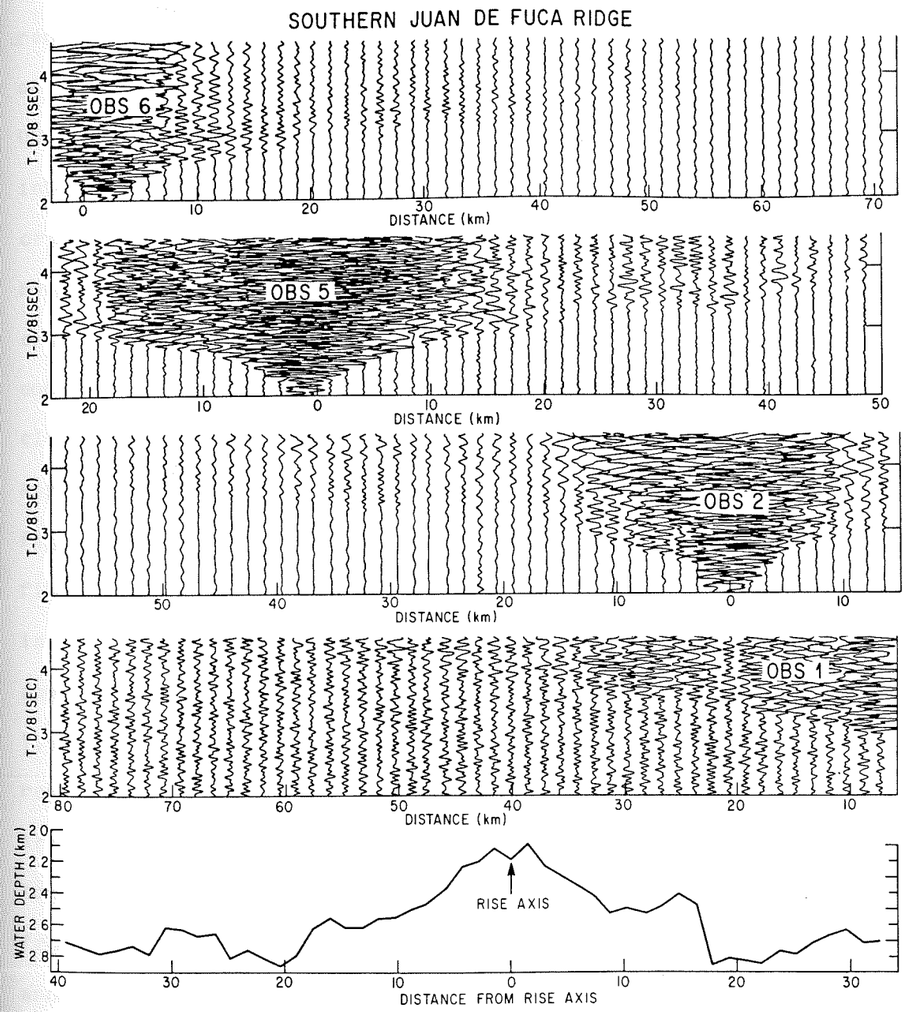

Figure 32. Ocean bottom seismometer refraction data from the southern Juan de Fuca. This data was collected on cruise TT-161 of the R/V Thomas G. Thompson. The second panel from the top shows the data for OBS 5. See Figure 3 for the refraction line (R_1) for this data.

during the shooting of line R_1. In Figure 32, the the full waveform recorded for each refraction shot is shown for the OBS's; the location of the OBS is at 0 kilometers distance, and shots to the west of the OBS are plotted to the right of the 0 kilometer point. Of particular interest is OBS 5 which was situated -22 kilometers east of the ridge crest along the refraction line. Arrivals from shots in the neighborhood of 40 kilometers to the west of OBS 5 bottomed in the crust beneath the ridge axis (also indicated in Figure 32) at depths corresponding to those of the reflector seen on Line 8A. There was clearly no delay of these arrivals, which would have traveled through any possible magma chamber associated with the reflector on Line 8A. Figure 33 shows back shooting ray paths for OBS 5, along with the best fitting velocity model for the area; the ray paths show the coverage in the area of interest. There is a slight velocity inversion at approximately 7 kilometers depth below sea level, but the drop from 7.0 to 6.9 kilometers per second is not nearly significant enough to represent molten material. In addition to this refraction data from Area A, similar data from Area B also indicate the absence of large bodies of molten material in the lower crust. Preliminary results from White and Clowes [1987] indicate that although small velocity anomalies may exist beneath the axis of the Endeavour segment, no large anomalous bodies are required by their data.

The reflector on Line 8A was the only feature on any of the six profiles in this thesis which was a likely candidate for a magma chamber. At this point it should be noted that a magma chamber may

Figure 33. Ray paths for two of the OBS's in Figure 32. A velocity model from the refraction data is also shown. OBS 5 is shown in the upper panel.

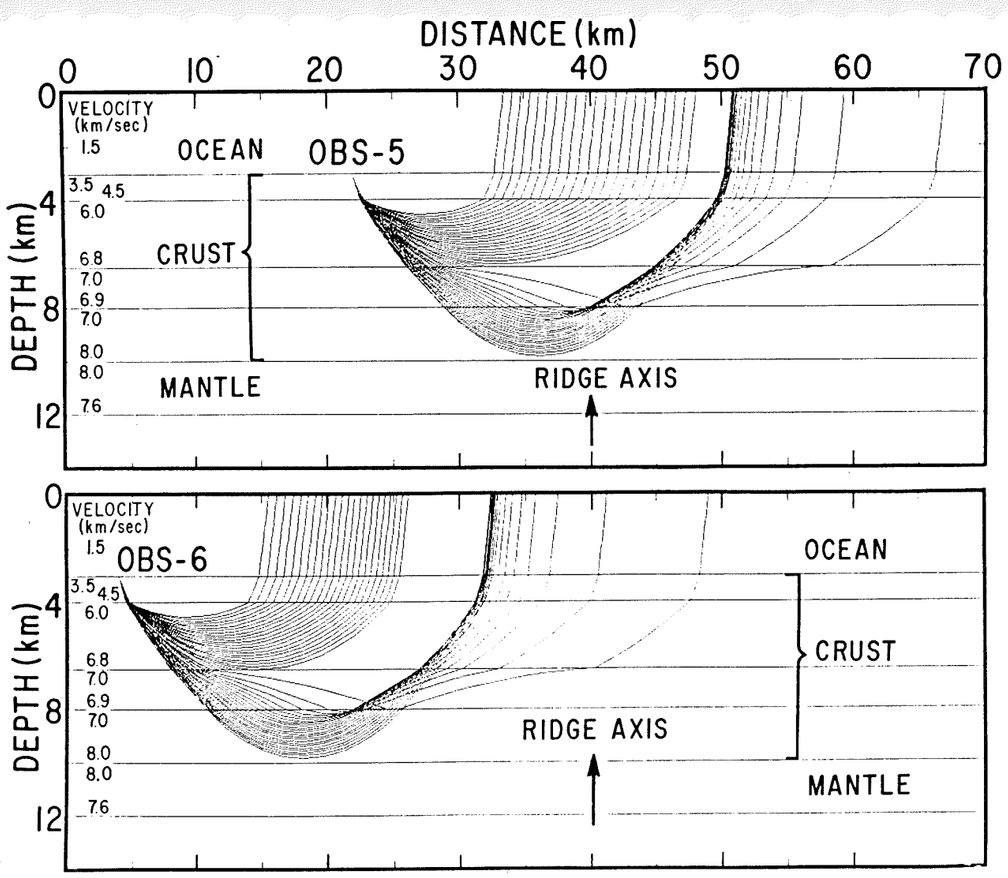

have been present, but not resolved. For example, the chamber could have been exceedingly narrow. One way to assess the limit of horizontal resolution of a seismic profiling system is through the use of Fresnel zones. Assuming a diffractive sea floor, the Fresnel zone is the area of sea floor which can reflect energy to the receiver within one-half cycle of the reflection; reflected energy within this time window will add constructively to the reflection [Sheriff, 1980a]. Bowen [1984] has shown that the size of the Fresnel zone depends on the experimental geometry, and that, compared to surface source and receiver geometries, deep towed geometries can offer approximately a 70% reduction in the width of the Fresnel zone. An estimate of the size of a Deep Tow Fresnel zone can be made by calculating the corresponding surface Fresnel zone and applying the reduction presented by Bowen [1984]. Using the approach of Sheriff [1980a], with a frequency of 12 Hz, an average (rms) velocity of 2.4 kilometers per second, and a surface geometry travel time of 3.5 seconds, the surface Fresnel zone for mid-crustal depths can be calculated to be ~650 meters in radius. Incorporating the 70% reduction of Bowen [1984], this gives a Fresnel zone with a radius of ~200 meters, or a diameter of ~400 meters. Sheriff [1980b] has shown that features less than one Fresnel zone in scale will appear as diffractions rather than as reflections. Migrating diffractions would collapse them to a point source, which would appear on the migrated section as an isolated wiggle. An isolated wiggle would, after the running stack, appear as just another laterally short feature, and

would be overlooked when examining the profiles. Thus a magma chamber less than roughly 400 meters wide would not be readily observed with the Deep Tow. A 400 meter wide magma chamber is exceptionally narrow: even ignoring hydrothermal advection, conductive cooling would soon solidify such a chamber. Such a small chamber would also have been hard to detect in seismic refraction experiments, but it is doubtful whether such a chamber could generate cumulate phases such as layered gabbros.

Alternatively, a magma chamber may be present, but the interface between it and the solid material overlying it could be extremely gradational, and thus not return a reflection. The point at which a boundary becomes too gradational to return a reflection depends on the wavelength of the seismic energy; if the boundary is thicker than roughly one wavelength, then the velocity contrast across the boundary would not produce a reflection. If seismic velocities in the rock above the chamber are on the order of 6 kilometers per second, given the peak spectral frequency of 12 Hz, the dominant wavelength would be 500 meters. A gradational boundary that was thicker than 500 meters would not be detectable with reflection techniques. Although no seismic reflection would be produced by such a boundary, if we assume that it represents a substantial velocity contrast and that the boundary has a reasonable horizontal extent (perhaps 1 - 2 kilometers), then it should have been detectable by the seismic refraction experiments mentioned above. No such feature was seen, or at least not one with a substantial velocity contrast.

Finally, a magma chamber may have been present, but filled with a partially solidified crystal mush. The detectability of such a feature is hard to assess, as it depends greatly on the amount of partial melt left, and on its distribution [ie. Mavko, 1980]. However, it is important to realize that such a chamber is likely well on its way to solidifying, and cannot be heavily relied on in an argument for a steady state magma chamber.

Arguments of the sort presented in the preceeding three paragraphs, supported by the refraction data mentioned earlier, lead to the conclusion that there is no firm evidence in this data set that a magma chamber exists on the JDF.

Figure 34 is a multichannel profile from Area B on the Endeavour segment of the JDF [Rohr et al., 1988; see Figure 6 for the track line of this profile]. This profile crosses the ridge crest at the same point as Line 3B (Figure 25) of this thesis. There are three features labelled on the multichannel profile; Moho, an axial relector, and an intermediate reflector. Although there are several reflectors on Line 3B which could correspond to the Moho reflector, none stands out obviously compared to the others. A similar situation exists for the axial reflector. The intermediate reflector on the multichannel profile corresponds very well however, to the series of reflectors that begins on Line 3B at a distance of 2.5 - 3 kilometers east of the axis, and at a depth below sea level of ~5.5 kilometers. The other numerous reflectors in the lower crust on Line 3B do not stand out on the multichannel profile, although they may be present as fainter

Figure 34. Migrated multichannel reflection data from the Endeavour Segment of the Juan de Fuca (From Rohr et al. [1988].)

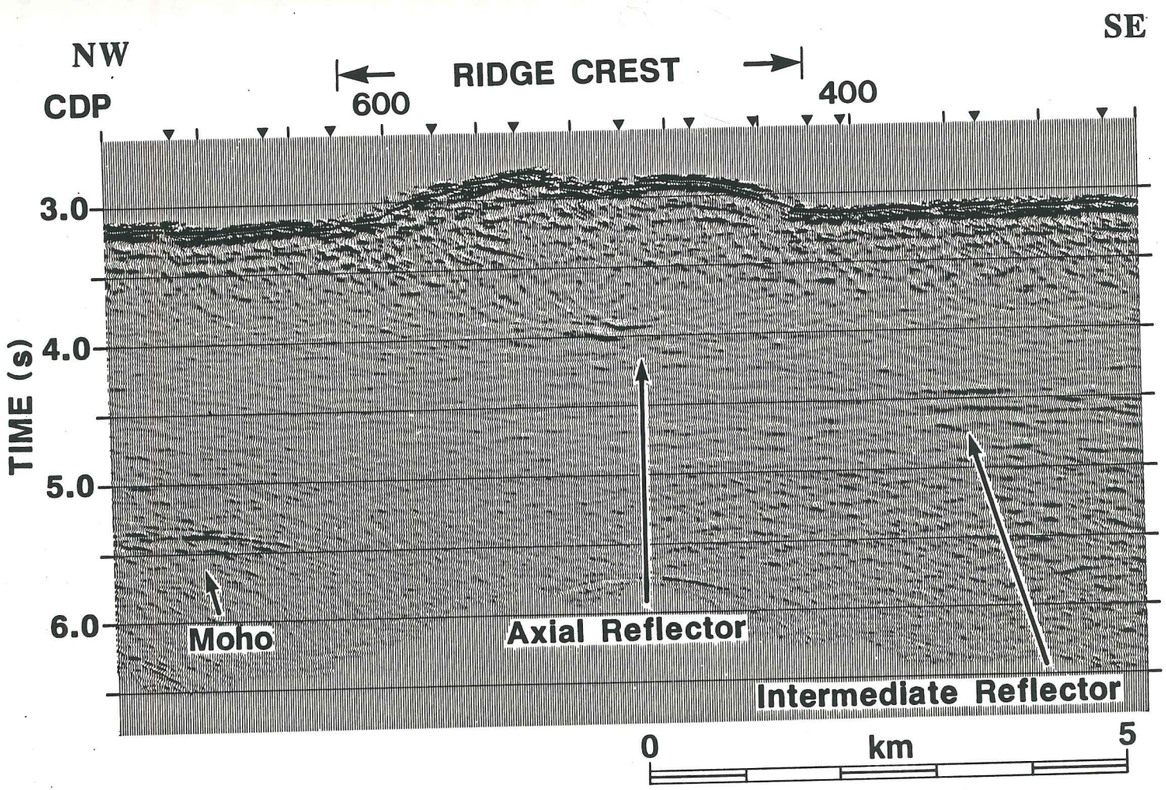

features. Rohr et al. [1988] do not interpret the axial reflector as a magma chamber; they were also unable to discern a polarity reversal. Instead they hypothesize that the reflector is related to a temperature anomaly, and they also attach a similar interpretation to the intermediate reflector.

The layering in the lower crust on the profiles in this thesis could be related to thermal effects, but other interpretations are possible. The basic structure of oceanic crust, as determined from drilling and the study of ophiolites, has several lithologic changes which could reflect seismic energy. For example, there is the transition from pillow basalts to sheeted dikes, from the dikes to isotropic gabbros, or the transition from isotropic to layered gabbros. Rohr et al. [1988] detected shallow reflectors on their multichannel profile which possibly represent the pillow basalt/sheeted dike transition (these reflectors do not appear on the multichannel profile as presented in Figure 34, which is a version of their data that was processed so as to bring out deeper events; the data in this thesis were also processed in this fashion). Pillow basalt thicknesses are typically 0.5 to 1.0 kilometer, and therefore the onset of layering in the profiles in this thesis is too deep to be the pillow/dike transition. Sheeted dikes vary from roughly 1.0 to 1.5 kilometers in thickness, which puts the base of the dikes at from 1.5 to 2.5 kilometers. Since the layering in the Deep Tow profiles starts at a depth of roughly 3.5 kilometers, even with the considerable uncertainties involved, the layering is still too deep to

represent the base of the sheeted dikes. Isotropic gabbros are usually between 0.5 and 1.0 kilometer thick, putting the transition from isotropic gabbros to layered gabbros at 2.0 to 3.5 kilometers, which is in general agreement with the depths of the onset of layering in the Deep Tow profiles.

The thickness scale of the apparent layers in the lower crust is on the order of 500 meters, and is much too thick to represent the fine scale (ie. centimeter to tens of centimeters) layering of felsic and mafic units in layered gabbros. If these reflections are from the gabbros, they might represent instead internal reverberations or resonance phenomenon, or perhaps reflections from larger scale variations in composition. One example of larger scale phenomenon would be the ~100 meter scale rhythmic layering of ultramafic phases seen in the Samail ophiolite [Smewing, 1981]. Another example would be the megalenses of ultramafic material described by Karson and Collins [1984] and Brocher et al. [1985], which present a considerable seismic velocity contrast, and would provide strong reflections. Mutter et al. [1985], working with multichannel data from the western North Atlantic, found a reflecting horizon at a similar depth to that found for the layering in the Deep Tow profiles. They have interpreted the horizon as being from the layered gabbro, although it should be noted that they only observed a single reflection from the top of the layered gabbros, and not a series of internal reflections.

The apparent layering in the lower crust presents the possibility of gaining insight into the scale of homogeneities, or perhaps magma

chambers on the JDF. The absence of permanent or steady-state magma chambers has already been indicated, but intermittent chambers are still quite likely, in fact required if the layering represents layered gabbros. Presumably, at some point after the solidification of a magma chamber, it would be split apart when a new magma chamber is emplaced. If this process were occurring, then the horizontal length scale of the lower crustal reflectors could represent a lower bound on the possible half-width of magma chambers at the ridge crest. Failing this, the length scale could be representative of the length scale of homogeneities in the lower crust, which could be related to second order processes in magma chambers, such as the generation of the ultramafic megalenses mentioned above. This horizontal length scale is easy to measure, and the results are shown in Table 8. This measurement has been performed only on the profiles from cruise TT-196; the profiles from cruise We8506a have been omitted because of noise contamination. In each of the profiles examined, the longest 20-25 reflectors were measured. When making these measurements, care was taken to correct for any exaggeration of the length scale due to processing, in particular the running stack performed after migration. The average length scale from the four profiles analyzed is ~0.5 kilometer. This gives a fairly narrow but not unreasonable magma chamber width of roughly 1 kilometer. It is interesting to note that this figure corresponds closely to the width of the small axial valley seen at the ridge crest in both Area A and Area B, which suggests a possible relation between magma chamber dimension and axial

Table 8. Horizontal Length Scales of Layered Features.

LINE[1]	NUMBER MEASURED	LONGEST (km)	SHORTEST (km)	AVERAGE[2] (km)
1B	23	0.81	0.28	0.63
3B	22	0.70	0.18	0.43
4B	22	0.78	0.28	0.51
8A	23	0.85	0.25	0.48

NOTES:
1. Lines 1A and 2A were not analyzed because of being severely contaminated with noise.
2. The average length scale for all lines combined is ~0.5 kilometer.

topography. Additionally, if the figure of 1 kilometer is combined with the total opening rate of the JDF of 6 cm/year, then the result is an average time interval of 17,000 years between the emplacement of magma chambers. This time interval agrees in order of magnitude with the values presented by Lister [1983, 1987].

Current Models of Crustal Generation

The final portion of this chapter is a discussion of the Deep Tow data as it relates to current models of crustal generation. In order to simplify the discussion, the models have been grouped into three main categories: those requiring steady state magma chambers; those that require only intermittent magma chambers; and those that revolve around ridge crest segmentation.

A number of workers have advanced models that involve steady state magma chambers. Several of these models are the result of petrological observations on ophiolites and mid-ocean ridge basalts, for example: Cann [1974]; Bryan and Moore [1977]; Dewey and Kidd [1977]; Pallister and Hopson [1981]; and Casey and Karson [1981]. Other researchers have developed steady-state models on the basis of thermal and mechanical conditions at mid-ocean ridges: Davis and Lister [1974]; Sleep [1975]; Kusznir and Bott [1976]. The models of all of these workers have the common theme of a steady state magma chamber, with occasional replenishment of the magma as spreading continues. The results of this thesis clearly conflict with all such models, as no firm evidence for a magma chamber has been found.

An example of the second sort of model of crustal generation is that of Lister [1983]. In his model, spreading and magma chambers are intermittent. Clearly the absence of a magma chamber in the Deep Tow data are consistent with such a model. In addition, Lister's model requires that hydrothermal venting be observed at ridge crests only after the solidification of magma chambers. The presence of active venting at both Areas A and B would tend to further corroborate Lister's model.

The final group of models of crustal generation is based on the observation that mid-ocean ridges are divided into numerous smaller segments. Examples of these models have been presented or supported by: Francheteau and Ballard [1983]; MacDonald et al. [1984]; Whitehead et al. [1984]; Schouten et al. [1985]; Langmuir et al. [1986]; and Detrick et al. [1987]. Many of these models involve a steady-state magma chamber only at the peak or summit of an individual ridge segment. Crustal generation is accomplished either by the intermittent injection of dikes laterally along strike on the segment, or by lateral inflation of a magma chamber. The Deep Tow data in this thesis are not compatible with this sort of situation, as the profiles from both Areas A and B are at or near the summit of the individual segments. This may not be entirely unexpected, however, as many of these models have been developed based on observations made on the fast spreading East Pacific Rise. Based on the data presented here, this last class of models would need to be modified somewhat to be applicable to the JDF.

Chapter 6

Summary

With the objective of determining crustal structure, and therefore gaining insight into the processes at mid-ocean ridges, six seismic reflection profiles were collected in 1985 and 1986; three from the southern JDF near 44° 45', and three from the Endeavour segment near 48°. Processing of the profiles included deconvolution, migration, and automatic gain control. The main features of the processed profiles are a relatively featureless upper crust, and a lower crust with numerous horizontally coherent features. These features do not appear to be processing artifacts, and do not appear to be related to other profiling complications such as P-S conversions, or high order multiples. The depth to the onset of the horizontal features is 3.5±0.5 kilometers. The main conclusions are threefold. First, there is no firm evidence for the existence of magma chambers on the JDF based on the data presented here. Second, a crustal transition has been imaged (the transition to the coherent horizontal features), which could correspond to the top of the layered gabbros. Third, the Deep Tow system is capable of imaging crustal structure at mid-ocean ridges, and is thus a useful tool for understanding mid-ocean ridge crest processes.

Bibliography

Atwater, T., Implications of plate tectonics for the Cenozoic tectonic evolution of western North America, Geol. Soc. Amer. Bull., 81, 3513-3536, 1970.

Berkhout, A. J., Least-squares inverse filtering and wavelet deconvolution, Geophysics, 42, No. 7, 1369-1383, 1977.

Bowen, A. N., A high-resolution seismic profiling system using a deep-towed horizontal hydrophone streamer, Mar. Geophys. Res., 6, 275-293, 1984.

Bracewell, R. N., The Fourier Transform and its Applications, 2nd ed., McGraw-Hill, New York, 444 pp., 1986.

Brigham, E. O., The Fast Fourier Transform, Prentice-Hall, Englewood Cliffs, N. J., 252 pp., 1974.

Brocher, T. M., J. A. Karson, and J. A. Collins, Seismic stratigraphy of the oceanic Moho based on ophiolite models, Geology, 13, 62-65, 1985.

Bryan, W. B., and J. G. Moore, Compositional variations of young basalts in the Mid-Atlantic Ridge rift valley near lat 36° 49' N, Geol. Soc. Amer. Bull., 88, 556-570, 1977.

Cann, J. R., A model for oceanic crustal structure developed, Geophys. J. R. Astron. Soc., 39, 169-187, 1974.

Casey, J. F., and J. A. Karson, Magma chamber profiles from the Bay of Islands ophiolite complex, Nature, 292, 295-301, 1981.

Carter, J. A., and L. N. Frazer, Rapid f-k migration of zero offset marine reflection data, J. Geophys. Res., 87, No. B11, 9365-9373, 1982.

Chun, J. H., and C. A. Jacewitz, Fundamentals of frequency domain migration, Geophysics, 46, No. 5, 717-733, 1981.

Davis, E. E., and C. R. B. Lister, Fundamentals of ridge-crest topography, Earth Planet. Sci. Lett., 21, 405-413.

Delaney, J. R., H. P. Johnson, and J. L. Karsten, The Juan de Fuca Ridge-hot spot-propagating rift system: New tectonic, geochemical, and magnetic data, J. Geophys. Res., 86, No. B12, 11,747-11,750, 1981.

Delaney, J. R., and M. K. Tivey, Geology of the Endeavour Segment of the Juan de Fuca Ridge, manuscript in preparation, 1988.

Detrick, R. S., P. Buhl, E. Vera, J. Mutter, J. Orcutt, J. Madsen, and T. Brocher, Multi-channel seismic imaging of a crustal magma chamber along the East Pacific Rise, Nature, 326, 35-41, 1987.

Dewey, J. F., and W. S. F. Kidd, Geometry of plate accretion, Geol. Soc. Amer. Bull., 88, 960-968, 1977.

Dixon, J. E., D. A. Clague, and J.-P. Eissen, Gabbroic xenoliths and host ferrobasalt from the southern Juan de Fuca Ridge, J. Geophys. Res., 91, No. B3, 3795-3820, 1986.

Francheteau, J., and R. D. Ballard, The East Pacific Rise near 21° N, 13° N, and 20° S: Inferences for along-strike variability of axial processes of the Mid-Ocean Ridge, Earth Planet. Sci. Lett., 64, 93-116, 1983.

Hale, L. D., C. J. Morton, and N. H. Sleep, Reinterpretation of seismic reflection data over the East Pacific Rise, J. Geophys. Res., 87, No. B9, 7707-7717, 1982.

Hatton, L., M. H. Worthington, and J. Makin, Seismic Data Processing; Theory and Practice, Blackwell Scientific Publications, Oxford, United Kingdom, 177 pp., 1986.

Herron, T. J., W. J. Ludwig, P. L. Stoffa, T. K. Kan, and P. Buhl, Structure of the East Pacific Rise crest from multichannel seismic reflection data, J. Geophys. Res., 83, No. B2, 798-804, 1978.

Herron, T. J., P. L. Stoffa, and P. Buhl, Magma chamber and mantle reflections - East Pacific Rise, Geophys. Res. Lett., 7, No. 11, 989-992, 1980.

Kanasewich, E. R., Time Sequence Analysis in Geophysics, The University of Alberta Press, Edmonton, Alberta, Canada, 352 pp., 1973.

Karson, J. A., and J. A. Collins, Geologic and seismic velocity structure of the crust/mantle transition in the Bay of Islands ophiolite complex, J. Geophys. Res., 89, No. B7, 6126-6138, 1984.

Kusznir, N. J., and M. H. P. Bott, A thermal study of oceanic crust, Geophys. J. R. Astron. Soc., 47, 83-95, 1976.

Langmuir, C. H., J. F. Bender, and R. Batiza, Petrological and tectonic segmentation of the East Pacific Rise, 5° 30' - 14° 30' N, Nature, 332, 422-429.

Lister, C. R. B., On the intermittency and crystallization mechanisms of sub-seafloor magma chambers, Geophys. J. R. Astron. Soc., 73, 351-366, 1983.

Lister, C. R. B., A physically self-consistent model of thermo-tectonics at spreading centers, in; Mid-Ocean Ridges - a Dynamic Global System, 62-75, Ocean Studies Board Commission on Physical Sciences, Mathematics and Resources; National Research Council; National Academy Press, Wash., D. C., 1988.

Macdonald, K. C., J.-C. Sempere, and P. J. Fox, East Pacific Rise from Siqueiros to Orozco Fracture Zones: Along-strike continuity of axial neovolcanic zone and structure and evolution of overlapping spreading centers, J. Geophys. Res., 89, No. B7, 6049-6069, 1984.

Mavko, G. M., Velocity and attenuation in partially molten rocks, J. Geophys. Res., 85, No. B10, 5173-5189, 1980.

Morton, J. L., and N. H. Sleep, Seismic reflections from a Lau Basin magma chamber, in Geology and Offshore Resources of Pacific Island Arcs - Tonga Region, Earth Sci. Ser., 2, edited by D. W. Scholl and T. L. Vallier, 441-453, Circum-Pcific Council for Energy and Mineral Resources, Houston, Tex., 1985.

Morton, J. L., N. H. Sleep, W. R. Normark, and D. H. Tompkins, Structure of the southern Juan de Fuca Ridge from seismic reflection records, J. Geophys. Res., 92, No. B11, 11,315-11,326, 1987.

Murase, T. and A. R. McBirney, Properties of some common igneous rocks and their melts at high temperatures, Geol. Soc. Amer. Bull., 84, 3563-3592, 1973.

Mutter, J. C., and the North Atlantic Transect (NAT) Study Group, Multichannel seismic images of the oceanic crust's internal structure: Evidence for a magma chamber beneath the Mesozoic Mid-Atlantic Ridge, Geology, 13, 629-632, 1985.

Normark, W. R., J. L. Morton, and S. L. Ross, Submersible observations along the southern Juan de Fuca Ridge: 1984 Alvin program, J. Geophys. Res., 92, No. B11, 11,283-11,290, 1987.

Pallister, J. S., and C. A. Hopson, Samail ophiolite plutonic suite: Field relations, phase variation, cryptic variation and layering, and a model of a spreading ridge magma chamber, J. Geophys. Res., 86, No. B4, 2593-2644, 1981.

Parkes, G., and L. Hatton, The Marine Seismic Source, D. Reidel, Dordrecht, Holland, 114 pp., 1986.

Robinson, E. A., and S. Treitel, Geophysical Signal Analysis, Prentice-Hall, Englewood Cliffs, N. J., 466 pp., 1980.

Robinson, E. A., Multichannel Time Series Analysis with Digital Computer Programs, 2nd ed., Goose Pond Press, Houston, Tex., 454 pp., 1983.

Rohr, K. M. M., B. Milkereit, and C. J. Yorath, Asymmetric crustal structure across the Juan de Fuca Ridge, Geology, in press, 1988.

Schouten, H., K. D. Klitgord, and J. A. Whitehead, Segmentation of mid-ocean ridges, Nature, 317, 225-229, 1985.

Sheriff, R. E., Nomogram for Fresnel-zone calculation, Geophysics, 45, No. 5, 968-972, 1980a.

Sheriff, R. E., Seismic Stratigraphy, International Human Resources Development Corporation, Boston, 227 pp., 1980b.

Sleep, N. H., Formation of oceanic crust: Some thermal constraints, J. Geophys. Res., 80, No. 29, 4037-4042, 1975.

Smewing, J. D., Mixing characteristics and compositional differences in mantle-derived melts beneath spreading axes: Evidence from

cyclically layered rocks in the ophiolite of north Oman, J. Geophys. Res., 86, No. B4, 2645-2659, 1981.

Stolt, R. H., Migration by Fourier transform, Geophysics, 43, No. 1, 23-48, 1978.

U. S. Geological Survey Juan de Fuca Study Group, Submarine fissure eruptions and hydrothermal vents on the southern Juan de Fuca Ridge: Preliminary observations from the submersible Alvin, Geology, 14, 823-827, 1986.

White, W. R. H., and R. M. Clowes, Juan de Fuca Plate crustal structure: Results from ocean bottom seismograph studies, Eos Trans. AGU, 68, No. 44, 1371, 1987.

Whitehead, J. A., H. J. B. Dick, and H. Schouten, A mechanism for magmatic accretion under spreading centers, Nature, 312, 146-148, 1984.

Wilson, D. S., R. N. Hey, and C. Nishimura, Propagation as a mechanism of reorientation of the Juan de Fuca Ridge, J. Geophys. Res., 89, No. B11, 9215-9225, 1984.